MNE 20 (2023) 100223

Contents lists available at ScienceDirect

Micro and Nano Engineering

journal homepage: www.sciencedirect.com/journal/micro-and-nano-engineering

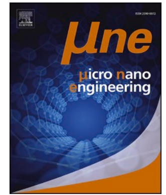

Ru/Ta bilayer approach to EUV mask absorbers: Experimental patterning and simulated imaging perspective

Devesh Thakare [a,b,*], Jean-François de Marneffe [b], Annelies Delabie [a,b], Vicky Philipsen [b,*]

[a] KU Leuven Department of Chemistry, Leuven, Belgium
[b] imec, Kapeldreef 75, B-3001 Leuven, Belgium

A R T I C L E I N F O

Keywords:
EUV lithography
EUV photomasks
EUV absorbers
Bi-layer patterning
Rigorous imaging simulations
M3D

A B S T R A C T

The optical properties and geometry of EUV mask absorbers play an essential role in determining the imaging performance of a mask in EUV lithography. Imaging metrics, including Normalized Image Log Slope (NILS), Telecentricity Error (TCE), and Best Focus Variation (BFV) through pitch deteriorate because of Mask 3-Dimensional (M3D) effects in EUV lithography, which limits the production efficiency. Alternative absorbers, including alloys of Ru and Ta, are anticipated to reduce some of the M3D effects; however, patterning these materials is challenging due to their low etch rates and poor etch selectivity against the Ru mask capping layer. Therefore, we propose a Ru/Ta bilayer approach to EUV mask absorbers and investigate it from a patterning and imaging standpoint. The top Ru layer thickness is calculated using the thin film interference phenomena, and we determine the bottom Ta layer that can produce improved NILS by utilizing the total absorber thickness optimization methodology. We demonstrate the patterning of the Ru/Ta bilayer using a two-step etch; the top Ru layer is patterned with Cl_2-O_2 Reactive Ion Etch (RIE), and the bottom Ta layer with Cl_2-N_2 RIE. The geometry and morphology of the patterned bilayer stack are investigated using TEM (Transmission Electron Microscopy), and interdiffusion at the interface of Ru and Ta is studied using EDS-STEM (Energy Dispersive X-ray Spectroscopy-Scanning Transmission Electron Microscopy). The non-ideal traits of the Ru/Ta bilayer stack, determined by experimental characterization techniques, are used to simulate the imaging performance and then compared against an ideal Ru/Ta bilayer stack, along with the reference Ta-based absorber. Even when non-idealities are considered, the simulation findings demonstrate that the Ru/Ta bilayer absorber exhibits improved NILS and reduced BFV compared to the Ta-based absorber. The outcomes encourage further research into the possibilities of multilayer absorbers, to tailor their optical characteristics by varying the thickness of individual layers.

1. Introduction

EUV lithography is being implemented into production for high-volume manufacturing by the semiconductor industry. EUV lithography employs reflective optics for pattern transfer, unlike transmissive optics used in the older generation of lithography. The state-of-the-art EUV mask consists of a Multilayer Mirror (ML) formed by alternate stacking of Mo and Si layers protected by a Ru capping layer and a patterned Ta-based absorber. The interaction of the EUV light with the mask results in the well-known M3D (Mask 3-Dimensional) effects. Consequently, the aerial image at the wafer level confronts challenges such as contrast fading (reduced Normalized Image Log Slope (NILS)), pattern shift through focus (also known as Telecentricity Error (TCE)), and Best Focus Variation (BFV) through pitch. The absorber material's refractive index, n, and extinction coefficient, k, significantly influence these aerial image metrics. Therefore, alternative absorber materials have been proposed in the literature to mitigate these M3D effects [1–3].

An alternative absorber could be categorized into a single layer or a multilayer absorber. A single layer can be further classified as a mono-element or an alloy absorber. Similarly, a multilayer absorber may have a stack of two or more mono elements, two or more alloys, or a combination of both. Simulation studies have demonstrated that low-*n* absorbers improve the imaging performance of EUV masks through NILS enhancement [3,4]. Ru is an element that is used as a capping layer by current EUV masks and is also categorized as a low-n material. The state-of-the-art EUV mask absorber is an alloy of Ta. Since Ru and Ta are the

* Corresponding authors at: imec, Kapeldreef 75, B-3001 Leuven, Belgium.
E-mail address: devesh.thakare@imec.be (D. Thakare).

https://doi.org/10.1016/j.mne.2023.100223
Received 9 January 2023; Received in revised form 27 July 2023; Accepted 5 August 2023
Available online 7 August 2023
2590-0072/© 2023 The Authors. Published by Elsevier B.V. This is an open access article under the CC BY license (http://creativecommons.org/licenses/by/4.0/).

materials that are known by the mask ecosystem, absorber materials consisting of these elements, either as a single alloy absorber or as a bilayer stack, are likely to behave as a low-n absorbers. Alloys of Ru and Ta have been previously investigated, which showed difficulty in patterning [5]. This paper studies the Ru/Ta bilayer absorber, and we motivate our investigation with two aspects: first, from a patterning standpoint and second, from an imaging standpoint.

Starting with the patterning standpoint, Wu et al. [5] reported low etch rates for RuTa alloy compared to typical hard masks (SiO_2 and Si_3N_4), which implies a requirement for thick hard masks or resist materials. This requirement makes it difficult to maintain the aspect ratio of mask features at the resolution limit. The smallest pitch target for a typical line and space (LnS) pattern at the mask level is expected to be 80 nm or below. The values correspond to the intended wafer level targets for High-NA (Numerical Aperture) 0.55 application with anamorphic imaging (wafer level target: 10 nm LnS with a pitch of 20 nm, industry goal by the year 2028) [6]. In addition, the etch selectivity of RuTa versus Ru is low [5]. This low etch selectivity may result in an over-etch of the Ru capping layer during the RuTa alloy etch process. The thickness of the Ru capping layer is critical as it is optimized for high EUV reflectivity in combination with the Mo/Si multilayer mirror. Thus, the patterning of RuTa alloys is challenging. We, therefore, propose a two-step absorber patterning process by splitting the absorber layer into two, with Ru on top and Ta at the bottom. The advantage is that a two-step etch process enables patterning to be adjusted for each layer separately, which overcomes the etch selectivity challenge concerning the underlying Ru capping layer. The top Ru layer is patterned with Cl_2-O_2 Reactive Ion Etch (RIE), and the bottom Ta layer is patterned with Cl_2-N_2 RIE.

Next, we will discuss the imaging standpoint by shedding some light on the complexity involved in the selection of the prospective EUV absorber and present our arguments for choosing a bilayer stack based on the literature review. The two key factors that the mask industry has been emphasizing for absorber thickness optimization are absorber reflectivity and phase shift induced by the absorber. These factors strongly depend on the absorber material's optical properties and thickness. The EUV reflectivity and the phase shift, exhibit swing behavior as a function of absorber thickness, and moreover, they are less likely to exhibit the local extremum at the same absorber thickness [7]. Also, this approach to absorber thickness optimization neglects the pattern and its dimension on the mask. Since the waveguide effect governs diffraction characteristics at sub-11 nm, Mesilhy et al. recommend concentrating on n, k, and thickness rather than transmission and phase [8]. In this study, the total absorber thickness optimization method prioritizes imaging metrics (primarily NILS) instead of absorber reflectivity and phase shift. NILS also exhibits a swing behavior as a function of absorber thickness. Hence, selecting an absorber thickness corresponding to a local maximum or minimum is essential to reduce the sensitivity toward thickness variations. Considering all these factors, identifying a single material that produces the desired imaging performance is challenging. The leading cause of this challenge is that all materials at 13.5 nm wavelength show a negligible difference between the real part of the refractive index of absorber materials and vacuum [9]. Moreover, the choice of absorber material is governed by many factors, such as compatibility with the existing lithography ecosystem, etch selectivity concerning the ML capping layer, stability over the operating temperature range, and in mask cleaning solutions. As a result, the range of materials that might be used as possible EUV absorbers is further constrained. Therefore, using two or more materials to obtain the desired characteristics of an absorber material is expected to prove beneficial. Either an alloy or a multilayer absorber stack could be used to accomplish it, each having its own advantages and disadvantages. An alloy absorber will result in a single-layer absorber with fixed optical properties restricted by its stable compositions, whereas in the case of an absorber with two or more layers, the optical properties can be tuned with the thickness adjustments of each layer [7]. A bilayer absorber requires a two-stage etch/repair process, whereas a single-layer absorber just needs one. Although Yan et al. [9] have discussed the bilayer approach in the literature before, the proposed thickness adjustment of the bilayer stack is based on the absorber's overall attenuation. The bilayer absorber in this study is addressed with an approach using the thin film interference phenomenon, explained in the subsequent section.

A variation of a multilayer or a bilayer absorber approach that has been encountered in literature is to use an etch stop layer beneath the primary absorber material. The purpose of this layer is to provide better etch selectivity concerning the underlying mask capping layer. The strategy that is typically utilized for such layers has a predetermined thickness, which is optimized to achieve the best possible etch results for the patterning process. Kang et al. [10] have reported the usage of TaBO as an etch-stop layer for Ru-based alloy absorbers. Another instance of a bilayer absorber encountered in literature involves using the bottom layer as a phase shifter [11]. The bottom Ta layer in our Ru/Ta bilayer stack can alternatively be thought of as an etch stop layer in addition to its primary purpose as an absorber layer. The distinctive aspect of our approach is that we regulate the thickness of the bottom layer to enhance the imaging performance while maintaining the thickness of the top layer to control the reflectance.

In addition, the low refractive index of Ru is expected to enable the guiding of light through the openings in the absorber [12].

Thus, to conclude, in this paper, we investigate the Ru/Ta bilayer as an alternative EUV absorber to check whether it can mitigate M3D effects. The geometry and morphology of the patterned bilayer stack are investigated using TEM (Transmission Electron Microscopy), and interdiffusion at the interface of Ru and Ta is studied using EDS-STEM (Energy Dispersive X-ray Spectroscopy-Scanning Transmission Electron Microscopy). The non-ideal traits of the Ru/Ta bilayer stack, determined by experimental characterization techniques, are used to simulate the imaging performance and then compared against an ideal Ru/Ta bilayer stack, along with the reference Ta-based absorber.

2. Methodology

This section discusses the approach employed for the Ru/Ta bilayer study. First, we will discuss the thin film interference phenomenon, which is the underlying principle for the bilayer absorber in this study. Next, we explain the step-by-step methodology applied for the experimental and simulation segment.

A schematic representation of thin film interference with a bilayer stack is shown in Fig. 1. The thickness of the top layer can be adjusted to form either a constructive or destructive interference between the light reflected from the top of the absorber (point A in Fig. 1) and the light reflected from the interface of the bilayer stack (point B in Fig. 1).

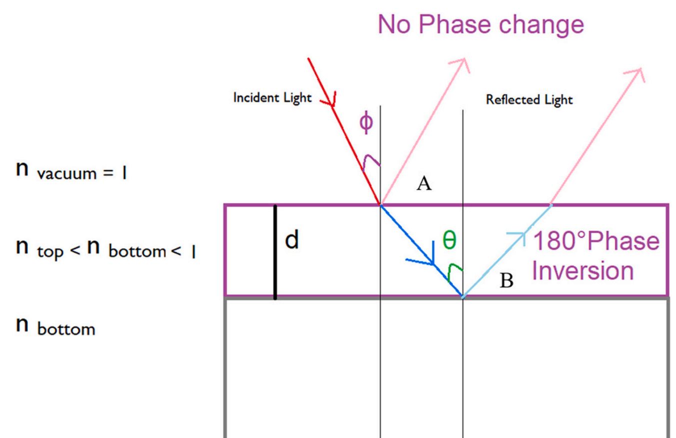

Fig. 1. Thin film interference phenomenon in a bilayer stack.

Depending on the relative values of *n* of the absorber materials at the bilayer interface, the reflected light will either experience a 180° phase inversion or not at all. Fig. 1 illustrates the phase of reflected light rays for the condition satisfying $n_{top} < n_{bottom} < n_{vacuum}$. The calculation of the top layer thickness that results in constructive or destructive interferences can be done using the formulas specified in Table 1.

with

n_{top} : refractive index of top layer material

n_{bottom} : refractive index of bottom layer material

d: the thickness of the top layer

λ: wavelength

f: angle of incidence (illumination source)

θ: angle of incidence at top/bottom layer interface (calculated using Snell's law).

m: order of the interference

Moving on to the step-by-step methodology, the chronology of the steps used for the approach is described below.

1. We fix the top layer thickness using the appropriate conditions based on the thin film interference principle. At this step, both constructive and destructive types have been investigated.
2. Next, we optimize the total thickness of the absorber, considering both top and bottom layers by prioritizing NILS.
3. Later we prepared the samples to test the etch feasibility of the bilayer stack determined in previous step. The main criterion of our interest is to have a good etch selectivity between the different materials during each patterning step in a multi-patterning etch process.
4. Furthermore, we characterize the patterned bilayer stack to create a simulation model by studying the oxidation layer, interdiffusion at the bilayer interface, and side wall angles.
5. Lastly, we evaluate the imaging performance of the modelled bilayer stack and compare it against an ideal Ru/Ta bilayer stack, along with the reference Ta-based absorber. The primary criteria considered are NILS, TCE, and BFV.

2.1. Top layer thickness optimization

As mentioned earlier, the top layer thickness resulting in either constructive or destructive interference can be obtained from the equations mentioned in Table 1. The values of optical constants for Ru and Ta at 13.5 nm wavelength are taken from the available S-Litho EUV database [13] and listed in Table 2. These values closely resemble the CXRO values [14]. Ru is primarily considered as a low-n material, but it is also a low-k material, which makes it suitable to be used as a top layer in a bilayer absorber stack. Since the fundamental phenomena of thin film interference is a surface phenomenon, lesser absorption of light by the top absorber, results in more interaction of the reflected light. The Ru/Ta bilayer stack with Ru as the top layer satisfies the condition $n_{top} < n_{bottom} < n_{vacuum}$.

2.2. Total absorber thickness optimization

Before moving to the total absorber thickness optimization, let us familiarise ourselves with the simulation settings used in this study.

2.2.1. Simulation setup

S-Litho EUV software from Synopsys® is being used in the study to simulate the imaging performance. S-Litho EUV performs rigorous EMF (Electro Magnetic Field) simulations while taking into account the topography of the mask and the optical characteristics of the mask materials. The typical simulation scanner inputs are a 13.5 nm EUV illumination source with a CRAO (Chief Ray Angle at Object) of 5.355° and a 20% radial obscuration in the centre in an anamorphic projection mirror [15,16]. All the imaging simulations are performed in the centre slit position for the CRAO. The Makhotkin et al. [17] published Mo/Si multilayer mirror mask model is used in these simulations. To account for an over-etch that can occur during the patterning of the absorber, a 0.5 nm recession of the Ru capping layer is considered in the mask trench region.

Table 1
Thin film interference.

Interference	$n_{top} < n_{bottom}$	$n_{top} > n_{bottom}$
Constructive	$2\, d\, n_{top} \cos\theta = (m - 1/2)\,\lambda$	$2\, d\, n_{top} \cos\theta = m\,\lambda$
Destructive	$2\, d\, n_{top} \cos\theta = m\,\lambda$	$2\, d\, n_{top} \cos\theta = (m - 1/2)\,\lambda$

Table 2
Optical Constants of the two elements at EUV wavelength of 13.5 nm as available in the S-Litho EUV database.

Element	*n*	*k*
Ru	0.886358	0.0170689
Ta	0.94291	0.04081

2.2.2. Bilayer absorber stack thickness optimization

Once the top Ru layer thickness is fixed, we initiate the total absorber thickness optimization process by varying the bottom Ta layer thickness. A Telecentric Sigma Point Source (TS-PS) corresponding to the smallest pitch of interest at the wafer level has been employed for absorber thickness optimization. For equal line and space patterns, the TS-PS can be determined by using Eq. 1. NILS has been considered as a primary criterion to determine the optimized absorber thickness. Using a TS-PS, we can exclude the focus variable from our simulations as NILS becomes independent of focus [18]. Thus, using a TS-PS illumination reduces the execution time during simulations. A higher NILS value indicates lower defectivity during the pattern transfer process [19]. The combination of mask bias and the absorber thickness that results in maximum NILS is used to plot the through-thickness behavior. A detailed absorber thickness optimization procedure has been presented in our previous study [20].

$$Telecentric\ \sigma\ for\ LnS = \frac{\lambda}{2\ NA\ P} \tag{1}$$

Where σ indicates the position of the point source in the pupil plane, λ denotes the wavelength of the illumination, NA is the numerical aperture, and P is the pattern pitch.

We have targeted horizontal LnS patterns, which are orthogonal to the CRAO, for thickness optimization in this simulation exercise. For horizontal LnS patterns, the direction of the mask feature topography is not parallel but orthogonal with the scan direction of the illuminator source of the EUV tool [21]. As a result, the imaging metrics of horizontal LnS patterns suffer the most from the shadowing effect [22]. This makes horizontal LnS critical, and therefore it has been given preferential treatment during thickness optimization. It is crucial to mention that shadowing also impacts other orientations since the light is incident on the mask patterns over a range of angles [21,22]. The extent of impact might not be as severe as in the case of horizontal LnS.

2.3. Sample preparation and etch study

In this section, we discuss the approach used to study the patterning of bilayer stack using an experimental sample. The first sub-section describes the conditions employed for the deposition of thin films. In the second subsection, the patterning of the Ru/Ta bilayer stack using Cl_2-O_2 RIE and Cl_2-N_2 RIE is explained, including hard mask schemes employed for the pattern transfer process. Furthermore, in the third subsection, methods used to remove hard mask is outlined.

2.3.1. Deposition of thin films

The initial aim was to study the etch rates of individual Ru and Ta

layers; therefore, respective thin films were deposited on a Si substrate using the Physical Vapor Deposition (PVD) process having a thickness of 50 nm. The etch rates were determined by measuring the thickness of the reference sample and the etched sample using XRR (X-Ray Reflectivity) analysis. For the second step, the sample required to demonstrate the patterning of the Ru/Ta bilayer was prepared after the absorber thickness optimization step. To mimic the EUV mask conditions on a 300 mm Si wafer, a thin Ru layer was deposited before the Ru/Ta bilayer stack deposition. A slightly thicker Ru layer of 10 nm instead of the normal 3 nm of mask capping layer was preferred, such that it becomes easier to detect a possible over etch of Ru while patterning the Ta layer. Considering the differences in the surface energies between the native oxide on the Si wafer and Ru, it could have resulted in the delamination of Ru thin film [23]. Therefore, a 2 nm of TaN adhesion layer was deposited under the Ru layer to prevent it from possible delamination.

After depositing the 10 nm Ru underlayer, the bilayer stack with the bottom Ta layer and top Ru layer was deposited using the PVD process at room temperature and 4.5e-4 Torr pressure without a vacuum break. A 5 nm of TiN was deposited through the PVD process on the top Ru layer as an adhesion layer for the hard mask stack to prevent it from unwanted delamination. The hard mask stack included 200 nm of Si_3N_4 followed by 50 nm SiO_2. The silicon nitride layer was deposited using a PECVD (Plasma Enhanced Chemical Vapor Deposition) process, and the silicon dioxide layer was deposited using the CVD (Chemical Vapor Deposition) process, both at a temperature of 180° C.

2.3.2. *Patterning of Ru/Ta bilayer*

The optimal plasma etching of Ru and Ta is based on Chlorine chemistry [24–26]. Pattern transfer requires the use of a mask that has a superior etch resistance than the target layer. The photoresist is a typical mask that can be patterned by optical lithography techniques; however, it suffers from low resistance to Plasma, especially if a high bias voltage and high O_2 flow are used, as in the case of the Ru and Ta etch processes used in this work. The use of an inorganic hard mask is therefore required, showing higher resistance than photoresist. A natural choice is going to silicon nitride and silicon oxide, which are less chemically reactive in Cl_2-based plasmas. As shown in the paper by Wu et al. [5], the etch rate of Si_3N_4 and SiO_2 in Ar/Cl_2 plasma remains high compared to RuTa alloy, indicating that a relatively large hard mask thickness is required for optimal pattern transfer.

Consequently, it was decided to opt for a bilayer hard mask composed of 200 nm Si_3N_4 (bottom) and 50 nm SiO_2 (top), as mentioned in the previous subsection. The litho recipe developed at imec was optimized to print an LnS pattern having a 100 nm line with a pitch of 200 nm. The pattern was printed into 105 nm photoresist using DUV (Deep Ultra Violet)-193 nm immersion lithography, then transferred onto spin-on glass (SOG, 30 nm) and spin-on carbon (SOC, 150 nm) layers, which were then used to open the SiO_2 / Si_3N_4 hard mask. All levels of masks (SOG, SOC, SiO_2, and Si_3N_4) were etched into a 300 mm Lam Research Exelan® Flex 45 CCP commercial system, using state-of-the-art Plasma etch processes. After SiO_2 / Si_3N_4 hard mask opening, all remaining resist and/or plasma polymer residues were stripped off by an in-situ O_2 plasma, followed by an 0.05% diluted HF dip for 20 s. The complete pattern transfer sequence is described in Fig. 2.

2.3.3. *Hard mask and adhesion layer removal*

Once the bilayer stack is patterned, the hard masks need to be removed in two steps: first, the silicon nitride layer, and second, the 5 nm TiN adhesion layer.

In the first process step, the HF solution, which is frequently employed as an etchant for removing Si compounds, was experimented with to remove the silicon nitride layer. Various HF concentrations were

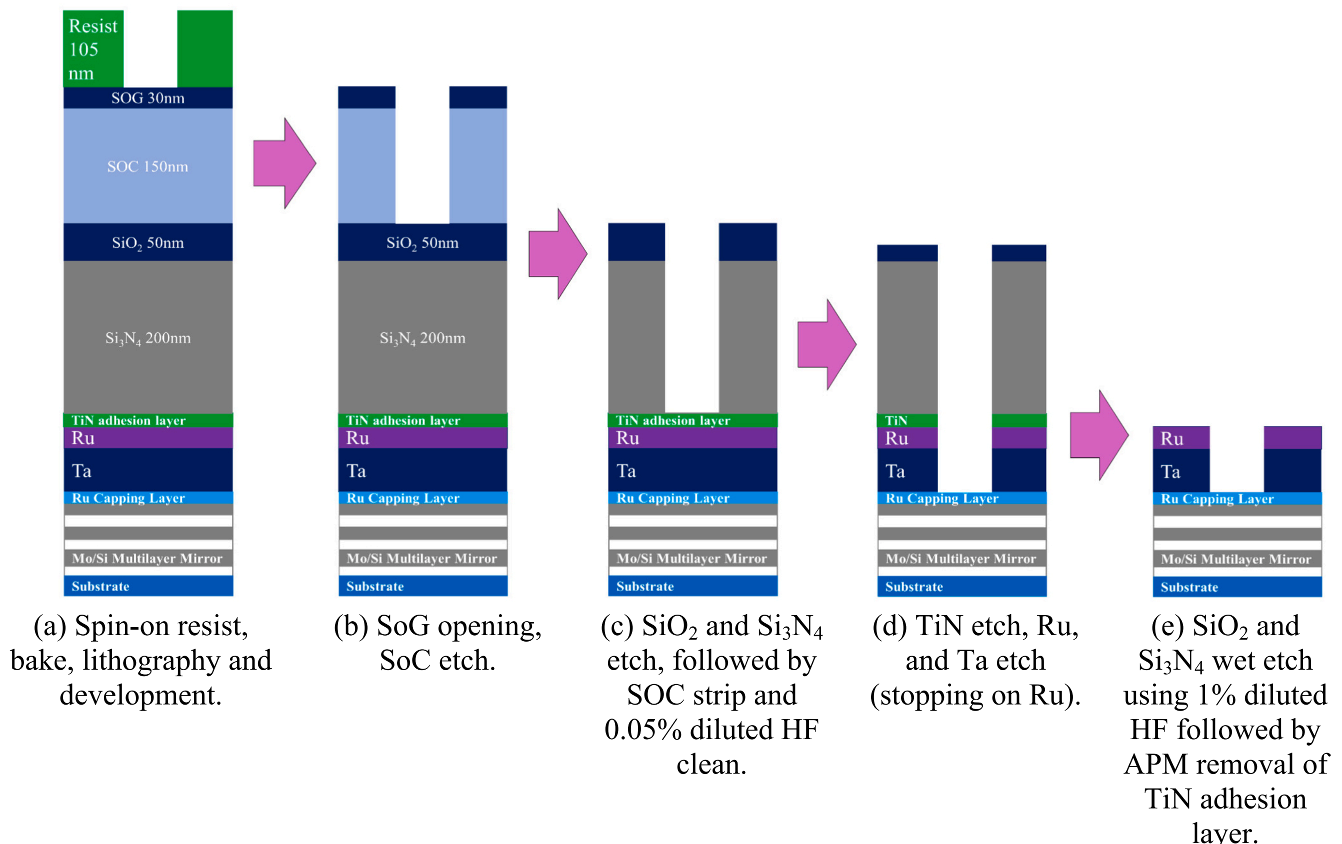

Fig. 2. Patterning sequence of Ru/Ta bilayer etch.

tested to see how well silicon nitride layer removal worked. The experiment included HF concentrations of 0.5%, 1%, and 2% and sample exposure times ranging from 30 s to 300 s, depending on the concentration. Patterned sample coupons of 2 cm × 2 cm were submerged in the beakers containing the different concentrations of HF solution.

In the second process step, the Ammonium Hydrogen Peroxide solution (also known as APM (Ammonium Peroxide Mixture)) was used to remove the TiN adhesion layer. This solution, which is popularly known as SC-1 (Standard Clean-1) is reported in the literature to etch Ti and TiN thin films [27]. The solution was prepared by mixing one part of ammonium and four parts of hydrogen peroxide in 20 parts of DIW (Deionised Water). The solution was maintained at 30° C using a hot plate, and the process screen time for samples was varied from 30 s to 120 s. Patterned sample coupons of 2 cm × 2 cm in size were immersed in the beaker containing APM solution to study this part of the experiment. After reviewing cross-sectional SEM (Scanning Electron Microscopy) images of each sample, the suitable condition for each process step was identified.

2.4. Experimental characterization of the bilayer stack

After the demonstration of patterning the Ru/Ta bilayer stack, we move on to its experimental characterization. A cross-sectional TEM analysis was performed on the patterned bilayer stack to study the morphology and side wall angle (SWA) profile. In addition, EDS-STEM is used to study the interdiffusion at the bilayer interface. Using this information, a bilayer stack profile that closely resembles the experimentally determined bilayer structure is modelled. This experimentally determined bilayer absorber stack model would be used to evaluate the imaging performance in addition to the ideal bilayer absorber stack. We thus intend to investigate the effects of non-idealities of the experimental mask pattern on the imaging metrics using experimental investigation findings discussed later in Sec. 3.5 (Imaging performance evaluation) and especially in Sec. 3.5.6 (contribution of individual non-idealities).

Since crystallinity affects the line edge roughness, a novel EUV absorber is expected to be either amorphous or nanocrystalline [28,29]. Therefore, to examine the crystallinity, a complementary X-Ray Diffractometry (XRD) analysis was performed on the unpatterned bilayer stack having no hard mask on top of it. The results obtained from XRD measurements were then compared with the High Resolution-TEM (HR-TEM) image analysis.

2.5. Imaging performance evaluation

Finally, we do a thorough-pitch analysis using the ideal and experimental bilayer stack models. The imaging performance of both is also compared with the reference Ta-based absorber. The imaging metrics that have been considered for through-pitch performance are NILS, TCE (Telecentricity Errors), also known as pattern shift through focus, and BFV (Best Focus Variation) through pitch. These metrics are evaluated at the Threshold-to-Size (TtS) anchored to the smallest pitch. The illumination source used for this simulation exercise is an inner half-leaf-shaped source (IHLDP) (Fig. 3 (a)). The tilt in the CRAO settings assumed for the simulations is such that when the light hits the mask, the lower pole makes a small incidence angle, whereas the upper pole makes a large incidence angle (Fig. 3 (b)). There are two main reasons to justify the selection of this illumination source shape. First, Franke et al. [18] recommend employing a dipole with either an inner or outer half-leaf shape to increase the NILS. Second, for the inner half leaf shape source, the two half poles are positioned nearer to the CRAO in comparison to the outer half leaf shape source. The reflectivity of an EUV mask depends on the incidence angle. This change in reflectivity through the incidence angle of light is defined as mask apodization [30]. Therefore, using an inner half leaf shape dipole that offers low incidence angles ensures a reduction in blocking of the diffraction orders by the absorber edge (reduced shadowing effect). Using inner half leaf shape dipole has the benefit of lowering TCE by reducing the imbalanced distribution of diffraction order intensities. The IHLDP illumination source is selected to reduce the mask apodization and M3D effects arising from it. The ultimate output is a function of the selected illumination source, the intrinsic characteristics of the EUV mask, and the settings of the exposure tool, which we aim to investigate.

The specifications used for the imaging metrics follow the suggested values in the literature. A NILS value larger than 2 is considered acceptable for efficient pattern transfer [31]. E. van Setten et al. [15] recommend maintaining TCE errors below 20 mrad to keep M3D-induced overlay errors under control. Mask bias and focus were varied simultaneously at fixed absorber thickness to find the right combination that prints on target with ±10% tolerance. The focus value that results

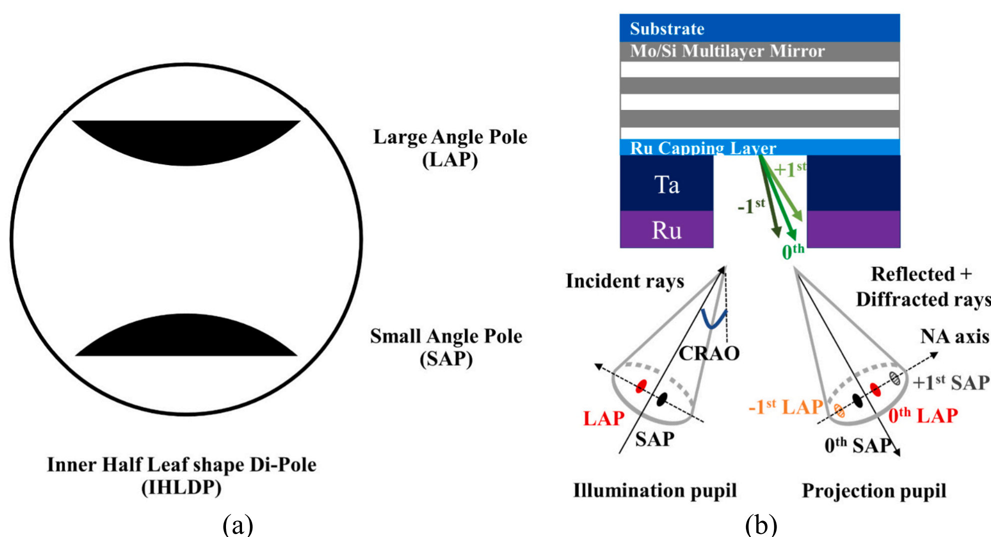

Fig. 3. A schematic representation of (a) Inner half leaf-shaped dipole (IHLDP) illumination source used for the through-pitch imaging comparison optimized to 20 nm pitch. The tilt in the CRAO settings assumed for the simulations is such that when the light hits the mask, the lower pole makes a small incidence angle (SAP (Small Angle Pole)) whereas the upper pole makes a large incidence angle (LAP (Large Angle Pole)). (b) a mask illuminated with a dipole highlighting the reflected plus diffracted rays captured by the projection optics. The number beside SAP/LAP label denotes the diffraction order corresponding to the respective poles that enter the NA.

in the maximum NILS is the best focus for a given pitch. The BFV is defined as the difference between the maximum and the minimum value of the best focus over a pitch range. The pitch values of the LnS pattern used for evaluating BFV range from 20 nm to 40 nm with an increment of 4 nm. Approximately 35 nm is the anticipated total focus budget for high NA EUV lithography, which is stringent compared to previous generations [32]. Therefore, to print the multiple pitches with the largest possible overlapping process window, the BFV should be as small as possible to ensure high-fidelity pattern transfer.

Another important aspect of the mask that needs to be mentioned is its tone. Depending on the reflective and absorber regions on an EUV mask, the tone of a photomask can be broadly classified either into a dark field or a bright/light field. Typically, in a dark field mask, a major portion of the ML mirror is covered with an absorber, whereas it is the opposite in the case of a bright field mask. Currently, a dark field mask in combination with a chemically amplified positive tone resist on the wafer is preferred in EUV lithography [33]. When a feature represented by the reflective area of a dark field mask is transferred onto a wafer coated with a positive tone photoresist, a trench is created at the wafer level after resist development. Some advantages of a dark field mask mentioned in literature are as follows; an extensive absorber coverage on a dark field mask makes it less vulnerable to defects present in the ML mirror beneath; in addition, it reduces heating and stray light in the scanner's optics [33]. Also, the dark field mask fabrication requires lesser processing steps in the present mask-making ecosystem. [33] Considering all these factors, the emphasis of our research is on dark-field imaging. However, this leaves the option open to investigate the imaging metrics using a bright field mask in combination with alternative absorbers in the future.

In addition to comparing the imaging metrics corresponding to the ideal and experimental Ru/Ta bilayer absorber profile, we also intend to study the impact of each non-ideality on imaging metrics. To address this aspect, we simulated only one non-ideality at a time and reported the percentage deviation observed in comparison to the ideal Ru/Ta bilayer absorber stack for the smallest pitch. This is supposed to shed light on which non-idealities have an influence in which manner and whether they can be mitigated during the deposition or pattering process.

The confidence in the simulator's results reflects through error bars. Therefore, the imaging metrics have been evaluated using different numeric settings of the S-Litho-euv software, ranging from low to high precision of evaluation that include four different settings for the rigorous calculation of the diffracted image viz. in a 5×5, 11×11, 21×21, and 51×51 rectangular grid distribution over the source pupil. The imaging metric plots represent the mean values with computed standard error.

Furthermore, to verify the accuracy of our simulations, we performed an additional exercise addressing the variations in optical constants and absorber thickness. To limit the number of simulations, we coupled the refractive index and extinction coefficient under the assumption that both of them either increase or decrease in terms of magnitude. Since experimentally determined optical constants for Ru and Ta layers were in agreement with the CXRO database, no huge deviations are expected [34,35]. Therefore, we have restricted the worst-case deviation to $\pm 2\%$ from the reported values (Table 2, Sec. 2.1). To account for variations in absorber thickness, the permissible ± 0.5 nm limit has been assigned [9]. The n, k, and thickness variations of both layers have been considered in the case of bilayer absorber stacks, whereas variations in only the bulk layer have been considered for the Ta-based absorber. We have restricted our exploration to only the LDP type of illumination source and the smallest pitch of 20 nm having a 10 nm target at the wafer level. We report mean values of the imaging parameters and estimated errors.

3. Results and discussions

3.1. Top layer thickness optimization

In this sub-section, we present the prospective thickness values for a top Ru absorber layer. As stated previously, the interference effect is profound for a top layer with a low-k material due to lower absorption, which is satisfied by Ru. Also, a thinner top-layer absorber is expected to contribute to increased interference. Therefore, for simplicity, the scope of this study has been restricted to first and second interferences only in order to demonstrate the patterning of the Ru/Ta bilayer stack. Ru satisfies the condition $n_{top} < n_{bottom} < n_{vacuum}$ in a Ru/Ta bilayer stack. Applying the appropriate formulas mentioned in Table 1, the top Ru layer that can generate respective interference is listed in Table 3. Our subsequent simulation-oriented research paper will address higher-order interferences corresponding to thicker Ru layers.

3.2. Total absorber thickness optimization

After determining the top absorber thickness using the thin film interference equations, we move on to total absorber thickness optimization through imaging simulations. Our simulation exercise targets horizontal line and space patterns with a 10 nm trench and 20 nm pitch at the wafer level using a TS-PS illumination. For High NA 0.55 application. Fig. 4 illustrates NILS as a function of total Ru/Ta absorber thickness for different top Ru layer thicknesses fixed to either constructive or destructive interference. The small swings through thickness result from interference of light reflected from the multilayer and the top of the absorber. It can be observed that Ru/Ta bilayer stacks exhibit a similar to improved performance in NILS when compared to RuTa alloy. The Ru/Ta bilayer stacks under consideration exhibit improved NILS at lower absorber thickness compared to the Ta-based absorber and are in close resemblance to the RuTa alloy. The top Ru layer's low *n* property results in a better balance between the diffraction order amplitudes of individual poles in a dipole illumination, which justifies the improvement in NILS [4,20]. Destructive interference shows a suppressed swing trend in comparison to constructive interference. The suppressed swing indicates a decreased sensitivity to thickness variations. Thus, the thickness sensitivity could also be controlled by tuning the top Ru layer thickness to the destructive interference.

As can be seen in Fig. 4, the NILS tends to saturate for absorber thicknesses >55 nm. This observed saturation in NILS is a consequence of many factors, such as the NA of the exposure tool and the absorber material's intrinsic optical properties that regulate the diffraction order amplitude and phase [20]. Although all Ru/Ta bilayer combinations under consideration exhibit promising NILS, we will restrict our simulation and patterning results to the Ru/Ta bilayer thickness corresponding to 2nd destructive interference, having a total thickness of 53.3 nm (15.3 nm of Ru on top of 38 nm of Ta layer). As stated previously, destructive interference has been given a preference as it is less sensitive to thickness variation. The absorber reflectivity and the induced phase shift by the selected absorber stack is addressed later in Sec. 3.5.2 and Sec. 3.5.7 respectively.

Table 3
Top layer Ru thicknesses for corresponding interferences at ϕ 5.355 deg.

Interference	Ru thickness (nm)
First Constructive	3.8
First Destructive	7.6
Second Constructive	11.5
Second Destructive	15.3

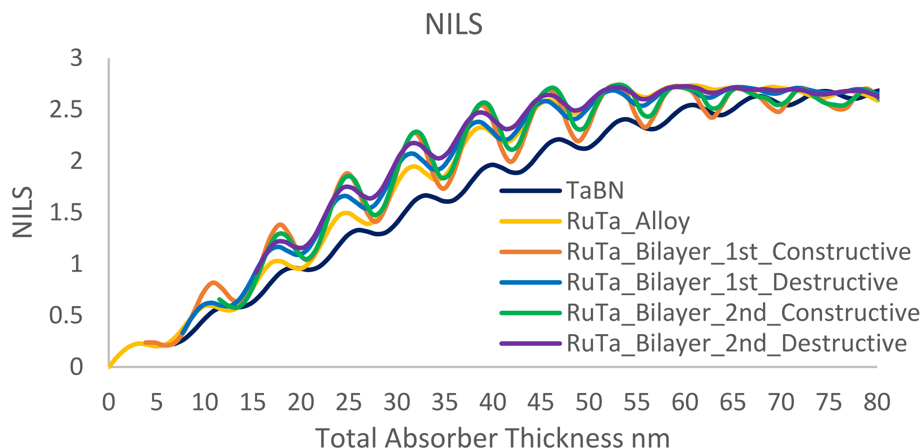

Fig. 4. NILS vs. absorber thickness plot for different absorber stacks, target: horizontal line and space pattern having 10 nm trench with a pitch of 20 nm using high NA EUV settings.

3.3. *Patterning of Ru/Ta bilayer*

In this sub-section, we will first discuss the etch rates of the Ru and Ta blanket thin films. Afterward, the patterning results for the bilayer stack will be described. Lastly, we will discuss the removal of hard masks.

3.3.1. *Etch rates determination of individual blanket thin films of Ru and ta*

Before demonstrating the etching of a bilayer stack, we determine the etch rates of blanket films with a starting thickness of 50 nm, using a Cl_2-O_2 (∼ 90% O_2) plasma chemistry for Ru and Cl_2-N_2 (∼ 60% N_2) plasma chemistry for Ta. Indeed, Ru's most volatile compound is RuO_4, which can be catalyzed by adding small amounts of Cl_2 [36]. On the other hand, Ta is better etched by pure Cl_2; however, the addition of N_2 leads to a higher Cl_2 dissociation into atomic chlorine, leading to a higher Ta etch rate [37]. The observed etch rates are listed in Table 4. For the Cl_2-O_2 RIE, we observe a high etch rate of Ru, but the Ta layer is not etched; only a thick surface oxide layer is formed (as observed by XRR, not shown). This is consistent with the formation of a Ta_2O_5-like layer which cannot be removed unless a Cl_2-rich plasma is used [38]. The Cl_2-N_2 RIE demonstrates a high etch rate for Ta compared to Ru, which is consistent with the inability to form RuO_4 volatile by-products without oxygen radicals in the Plasma. These results show the excellent etch selectivity of one metal against the other for these two plasma processes. We can therefore consider separating the patterning of the Ru/Ta bilayer in two subsequent Plasma etch steps. An absolute prerequisite is for the latter to be highly selective to the underlying ∼3 nm Ru cap (meant for protecting the Mo/Si multilayer mirror). The first etch step is the Cl_2-O_2 Plasma, to open the Ru film selectively to the underlying Ta; the second step uses the Cl_2-N_2 to etch the Ta layer selectively to the underlying Ru capping layer.

3.3.2. *Plasma etch processes for pattern transfer*

Fig. 5 shows cross-section SEM inspections after different steps of the Ru/Ta etch sequences for the bilayer stack consisting of 15.5 nm Ru on top of 38 nm Ta. Essentially, three layers must be etched, from top to bottom: starting with the 5 nm TiN adhesion layer, then the Ru, and finally, the Ta. The main components of the etch steps are described in Table 5 Etch step components. At first, the TiN is etched using similar plasma conditions as used for Ta, as titanium shows chloride by-products ($TiCl_4$) of higher vapor pressure than $TaCl_5$; CH_4 is added for sidewall passivation (avoid horizontal recess). After that, the Ru is etched by means of the Cl_2-O_2 described above, using first a break-through step aiming at removing Ti and Si residues. As seen in Fig. 5(b), vertical sidewalls are achieved with a flat etch front, corresponding to the landing on the Ta layer. The next stage of the patterning process consists of the Ta etch, which is performed by means of a Cl_2-N_2-based RIE, added by CH_4 for sidewall passivation; a breakthrough step is necessary, using BCl_3 to open the TaO_x layer formed by the previous etch step (high flow of O_2). Fig. 5(c,d) show the profile morphology of the structures after applying 45 s or 90 s of Ta main etch. In both cases, the tantalum layer is entirely removed, landing on the bottom Ru. Even for 90 s Ta etch, the bottom Ru is not recessed, confirming that the Cl_2-N_2-based RIE has a high selectivity toward Ru. Through the complete Ru/Ta etch sequence, it can be observed that the SiO_2/Si_3N_4 hard mask is only slightly eroded, opening the possibility to reduce its thickness for tighter pitches.

Table 4
Etch rates of Ru and Ta blanket thin films.

Etch Chemistry	Ru etch rate (nm/min)	Ta etch rate (nm/min)
Cl_2-O_2 RIE	75	∼0
Cl_2-N_2 RIE	0.31	67.2

3.3.3. *Hard mask and adhesion layer removal*

After patterning the bilayer stack, we investigate the removal of the SiO_2 /Si_3N_4 hard mask in diluted HF solutions with varying HF concentrations (see section 2.3.3). The results are presented in Fig. 6. The concentration of the HF solution is mentioned on the left, and the respective sample process time is indicated on each image. Low HF concentrations were used as it was found that 49% HF etches the Ta layer very fast, leading to stack delamination and absorber deterioration. The SiO_2 /Si_3N_4 hard mask can be removed completely by extending the diluted HF process time (Fig. 6). The time required to remove the hard mask decreases with increasing HF concentration. Wet etch is often regarded as isotropic, as we see an attack from the top as well as the sides. This is consistent with the layer-by-layer removal process suggested by Knotter et al. [39] The Si_3N_4 surface undergoes several intermediate transitions, including substitution by the -NH_2 group, until all Si-NH_2 bonds are replaced by Si—F. The silicon nitride etch rates indicate a complex nonlinear relationship between concentration and temperature [39]. It was decided to use a 1% HF recipe with 300 s to clean the silicon nitride hard mask on the remaining patterned wafers, ensuring long enough over-etch to clean any nitride residues, as well as reduced variability on dip time.

In the final step, the patterned samples, from which the silicon nitride hard mask has been removed, are then subjected to the removal of the TiN adhesion layer. This is performed by means of an ammonia peroxide mixture (APM) consisting of a 1:4:20 mix ratio of NH_4OH, H_2O_2, and H_2O at 30 °C, showing high selectivity to both the Ta and Ru layers. A processing screen time of 45 s was found to be sufficient to

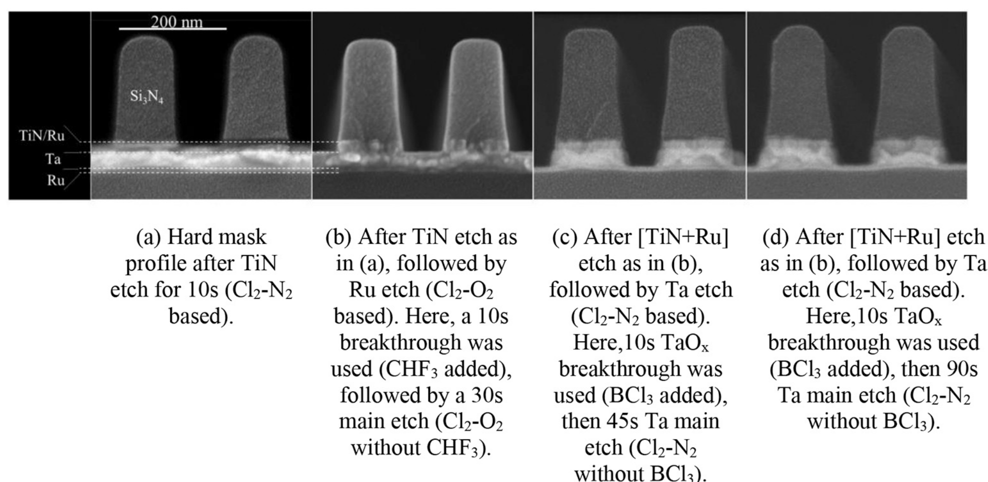

(a) Hard mask profile after TiN etch for 10s (Cl_2-N_2 based).

(b) After TiN etch as in (a), followed by Ru etch (Cl_2-O_2 based). Here, a 10s breakthrough was used (CHF_3 added), followed by a 30s main etch (Cl_2-O_2 without CHF_3).

(c) After [TiN+Ru] etch as in (b), followed by Ta etch (Cl_2-N_2 based). Here,10s TaO_x breakthrough was used (BCl_3 added), then 45s Ta main etch (Cl_2-N_2 without BCl_3).

(d) After [TiN+Ru] etch as in (b), followed by Ta etch (Cl_2-N_2 based). Here,10s TaO_x breakthrough was used (BCl_3 added), then 90s Ta main etch (Cl_2-N_2 without BCl_3).

Fig. 5. Pattern transfer into 15.5 nm/38 nm Ru/Ta bilayer deposited on 10 nm Ru (bottom). Note that XSEM was performed on different locations of the 300 mm wafers, highlighting the non-uniform character of the Si_3N_4 hard mask thickness (non-uniformity of the CVD process).

Table 5
Etch step components.

Step	Etch chemistry (Main components)	Goal
TiN etch	Cl_2-N_2-CH_4	Etch TiN, sidewall passivation
Ru breakthrough (BT)	Cl_2-O_2-CHF_3	Breakthrough Si_3N_4/TiN residues
Ru main etch (ME)	Cl_2-O_2	Ru etch, stop on Ta
Ta breakthrough (BT)	Cl_2-N_2-CH_4-BCl_3	Etch TaO_x formed by Ru etch
Ta main etch (ME)	Cl_2-N_2-CH_4	Etch Ta, stop on Ru

remove the TiN adhesion layer (Fig. 7).

3.4. Experimental characterization of the bilayer stack

Next, we discuss the experimental characterization of the Ru/Ta bilayer stack that corresponds to the second destructive interference. In the initial part, we discuss the TEM-EDS analysis of the patterned bilayer stack. In the later part, we discuss the crystallinity of the bilayer stack by comparing the data obtained from XRD measurements and TEM image analysis.

3.4.1. TEM-EDS analysis of the patterned bilayer

A cross-sectional TEM analysis of the patterned bilayer stack with a hard mask is displayed in Fig. 8. The image corresponds to a line and space pattern with a pitch of 200 nm. Although it failed to achieve an equal line and space pattern, the patterning is well-defined with an almost vertical sidewall angle. The duty cycle of the pattern could be further optimized by tweaking the litho process and thickness of the hard mask. The side wall angle is around 85°. A 5 nm thick Ta-oxide layer is present along the vertical side wall. The composition was confirmed by EDS analysis, as shown in Appendix A. The interdiffusion at the Ru—Ta interface is highlighted in the EDS line scan along the cross-section of a TEM sample (Fig. 8 (c)). The interdiffusion at the Ru/Ta bilayer interface is estimated to be 5 nm thick. A strong signal of Si presence in the bottom Ta layer is suspected due to a close resemblance between Ta M_v edge and Si K edge energies [40]. Therefore, the Ta signal is likely to be misinterpreted as the Si signal in the EDS line scan evaluation as it was not deconvoluted. A Cl signal detected in the Ru layer is suspected to be a consequence of Cl diffusion during the Ta etch process that uses Cl_2 RIE. It is anticipated that the presence of Cl will cause a change in the top Ru layer's optical characteristics [40,41]. $RuCl_3$ is a known compound whose XPS spectrum has been studied by McEvoy [42]. The photon energy of EUV light is about 92 eV, which is not close to any of the core levels of $RuCl_3$ [42]. Therefore, should $RuCl_3$ develop in the top layer, no significant difference is expected in the absorption coefficient of the top Ru layer. The refractive index of Cl is

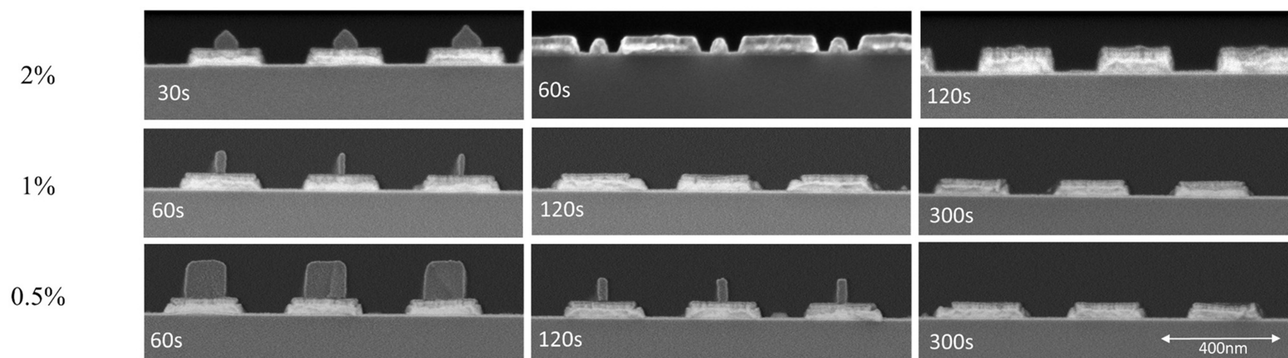

Fig. 6. Cross-section SEM images after hard mask removal with diluted HF dip of patterned Ru/Ta bilayer. HF concentrations are mentioned on the left, and the respective sample process time in seconds (s) has been indicated on each image. The cross-section SEM images correspond to a pitch of 400 nm. The image 2% HF / 60s suffers from an artifact due to Si_3N_4 mask residues (incomplete etch), leading to a Ru/Ta stripe in the middle of the trench.

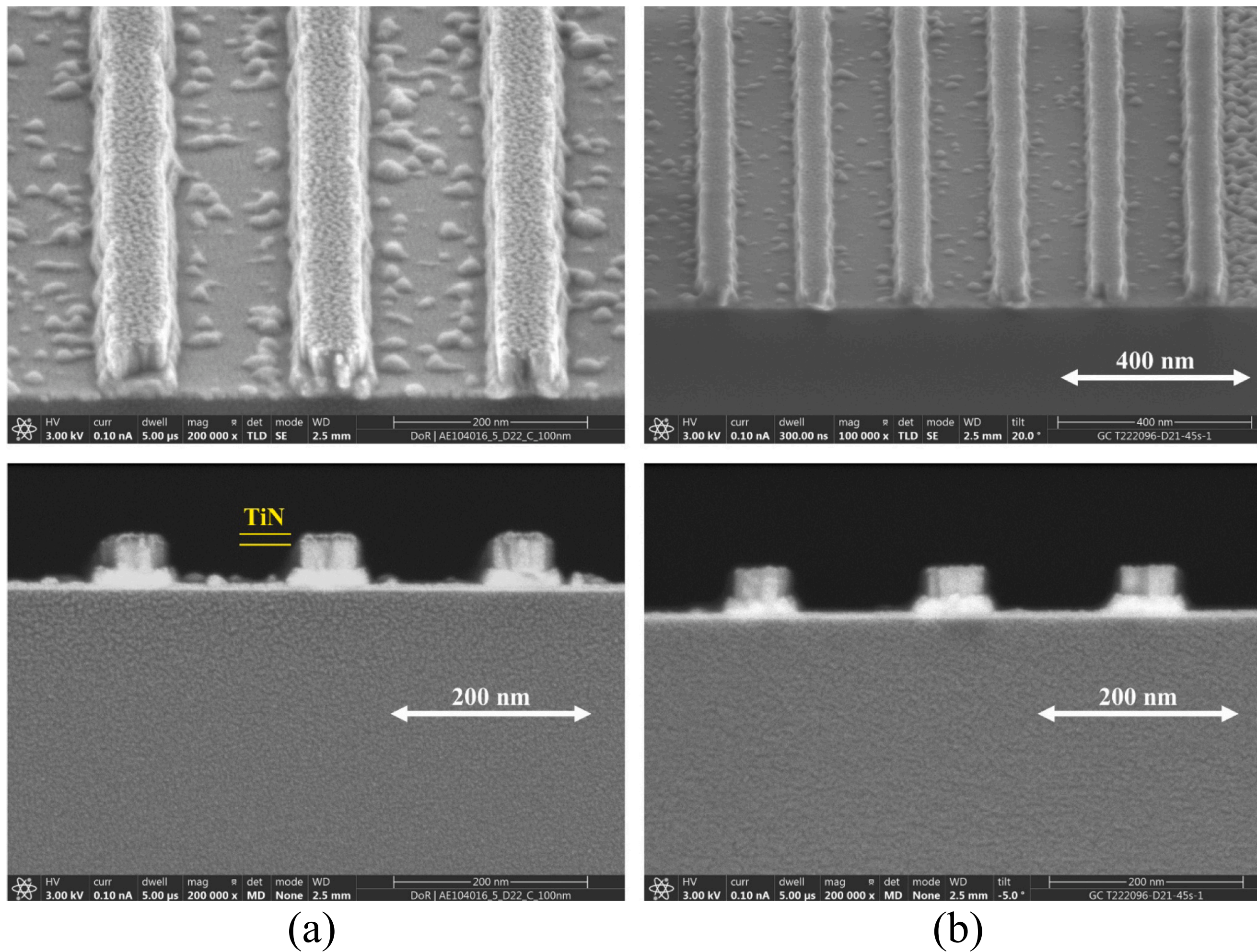

Fig. 7. Top-down and cross-section SEM images (a) before and (b) after 45 s of processing the Ru/Ta bilayer sample coupons with APM solution corresponding to 200 nm pitch of line and space structure. The residues observed between the lines are suspected due to improper etch of this sample wafer.

close to 1, and its extinction coefficient is negligible in the EUV range. As a result, the *n* value of the top Ru layer with the presence of Cl is expected to show an increment without much impact on its absorptive properties, as stated earlier. The detailed optical properties of the Ru layer with the presence of Cl are outside the scope of this work and may be addressed in a separate study. Thus, for simplicity, *n* and *k* values of Ru without Cl presence have been used for simulation (Table 2).

3.4.2. *Study of the bilayer stack's crystallinity*

We determine the crystallite size using two approaches; first, we use the XRD spectrum, and second, we do a visual analysis of the HR-TEM image. In Fig. 9, we compare the XRD spectrum of the Ru/Ta bilayer stack with the XRD plot of Ru and Ta powder, generated using an online app provided by Materials Project [43]. In addition, XRD data of the RuTa composite have also been considered for comparison. Peak 2 (2θ 38.435^o) can be linked to Ru (10−10) (2θ 38.385^o), and peak 4 (2θ 42.079^o) can be linked to Ru (0002) (2θ 42.345^o) hexagonal lattice structure. Although peak 4 is near the RuTa composite peak, we do not consider that related because no thick crystalline structures are observed in the TEM images (Fig. 8) at the bilayer interface. Peak 3 (2θ 38.682^o) can be assigned with Ta (110) (2θ 38.464^o). As we compare the XRD spectrum of a powder with that of a thin film formed on a substrate, the mismatch between the intensities can be attributed to the preferred crystal growth during the deposition, which results in a non-random orientation of crystallites [44,45]. Peak 1 (2θ 33.807^o) remains unidentified; the shift makes us uncertain as to whether it is related to the Si (002) (2θ 33°) substrate. When calculating crystallite sizes, the other minor peaks were ignored.

The crystallite sizes were determined using the online calculator service offered by instanano [50]. The crystallite size calculated using Scherrer's equation is the grain thickness perpendicular to the crystal planes [51]. This indicates that, in our case, the values obtained correspond to the crystallite size in the vertical direction of the thin film. The deconvolution and fitting of the peaks were done using Origin software [52]; the obtained parameters and calculated crystallite sizes are listed in Table 6. The crystallite size values obtained in the vertical direction are close to the respective thickness of individual layers in a bilayer stack.

In the second approach, the crystallite size along the horizontal direction was measured by visual analysis of the HR-TEM image (Fig. 10 (a)) using ImageJ [53]. Observing the HR-TEM image, the polycrystalline columnar orientation in the Ta layer can be visually confirmed. A histogram and normalized distribution plot of random measurements with calculated mean and standard deviation (SD) are displayed in Fig. 10 (b)&(c). The average crystallite size in the Ru layer is 11.76 nm (± 0.48), whereas that in the Ta layer is 15.05 nm (± 0.66). The crystallite size values obtained in the horizontal direction could be regarded as significant when compared to the dimensions of the smallest LnS pattern expected on a EUV mask (considering 40 nm lines with 80 nm pitch on the mask, corresponding to a 10 nm target having a pitch of 20 nm at wafer level). As mentioned earlier, a novel absorber material must be either amorphous or nanocrystalline; however, the literature

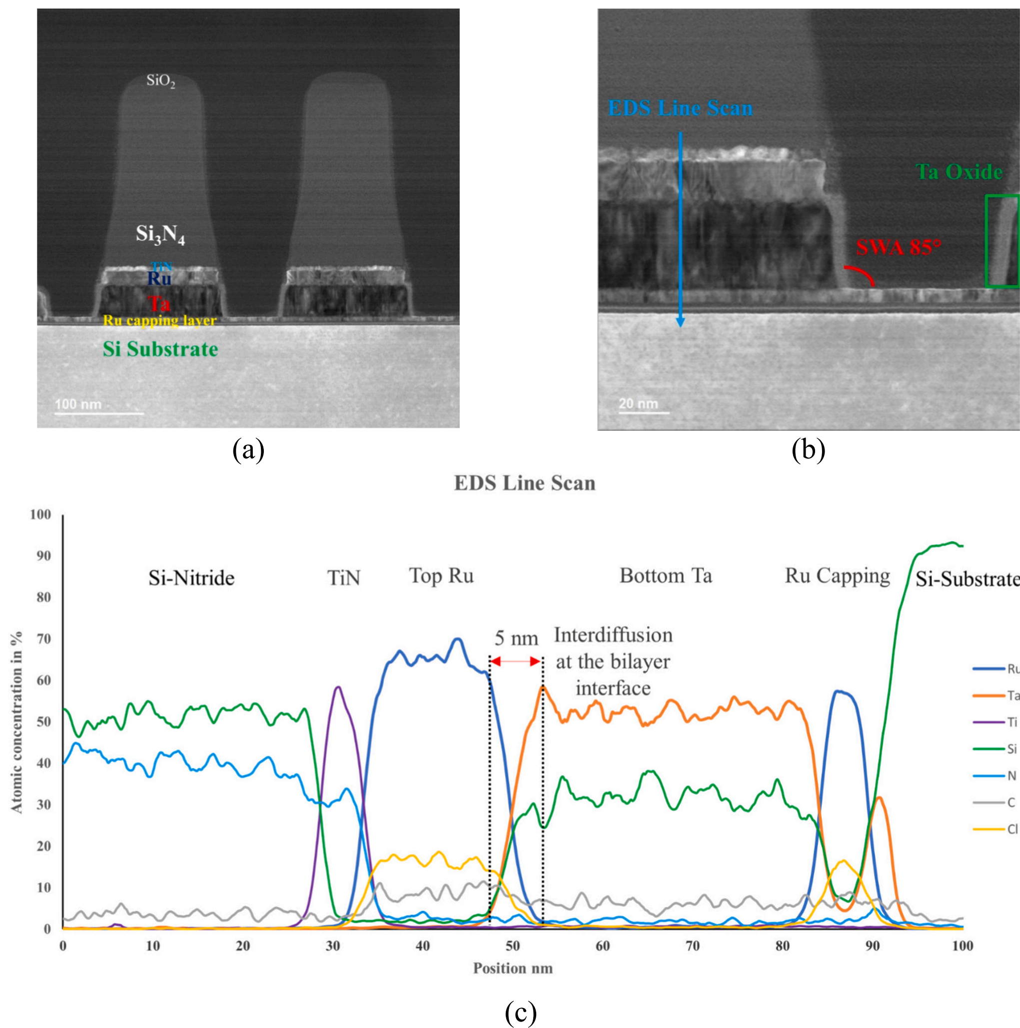

Fig. 8. (a) TEM cross-sectional view after bilayer etch with the hard mask still present for 2nd destructive absorber stack with 15.5 nm of Ru on top of 38 nm of Ta etched with two steps etch process (b) zoomed view of) TEM cross-sectional highlighting the SWA and Ta oxide along the side wall (c) Interdiffusion at the bilayer interface highlighted in the EDS line scan along the cross-section of a TEM sample, displaying atomic concentrations in percentage.

has not clearly defined any benchmarks for crystallinity. Luong et al. [54] considered a columnar grain structure having a 10 nm size, spanned over the entire Ni absorber layer, and reported a small impact on imaging compared to a single grain. Shimomura T. et al. [55] proposed alloyed Ru (a-Ru) as a capping layer that demonstrated better durability than pure metallic Ru film. Their approach can be used to decrease the crystallinity as alloyed Ru is generally expected to have reduced grain boundaries than pure Ru. Similarly, different techniques must be explored to regulate the crystallinity during Ta deposition. Furthermore, the impact of the 10 nm Ru underlayer on the growth of Ta crystallization is not addressed as it goes beyond the scope of this paper.

3.5. Imaging performance evaluation

In this section, we evaluate the imaging performance of the Ru/Ta bilayer and compare the performance to the reference Ta-based absorber. Before proceeding to the simulation results, we discuss the two absorber model stacks for the Ru/Ta bilayer. Next, TtS and mask bias values required to evaluate the imaging metrics are discussed. Later, the specifics of each imaging metric are covered. Lastly, we analyse the impact of each mask non-ideality on imaging metrics.

3.5.1. Mask model

Using the information obtained from the experimental characterization, an absorber model that closely resembles the actual bilayer stack was considered for the simulation exercise. In Fig. 11, the left model represents the ideal profile scenario, whereas the right model closely resembles the experimental results described in the previous section. The interdiffusion at the bilayer interface of about 5 nm is taken into consideration while designing the experimental profile. For simplicity, the optical constants for this interdiffusion layer may be approximated to the RuTa alloy, as reported by Wu et al. [5], which is listed in Table 7. Similarly, we also consider a 5 nm of Ta oxide layer along the side wall with an inclination of 85°, resembling the TEM results. Note that we do not expect this Ta-oxide layer to disappear completely during the hard mask removal, as the concentration of HF during hard mask removal is relatively low [56,57]. Moreover, Ta_2O_5 coating on electrodes as an HF barrier (protection layer) has been proposed in the literature [58]. Therefore, it is reasonable to consider an oxide layer of Ta along the side walls to understand the effects of a non-ideal structure. The model also considers a 1.2 nm Ru oxide layer at the Ru top surface and on the Ru sidewalls. This is in line with our group's previous XPS analysis (not shown) of a Ru blanket layer, which reveals a 1.2 nm ± 0.5 nm thick Ru oxide layer. The optical constants for these layers were taken from the CXRO database [14] and are listed in Table 7. The trench dimensions mentioned in our experimental model are measured at the opening of the trench, and the trench narrows toward the bottom. To simplify the complexity, the roughness at the surface and

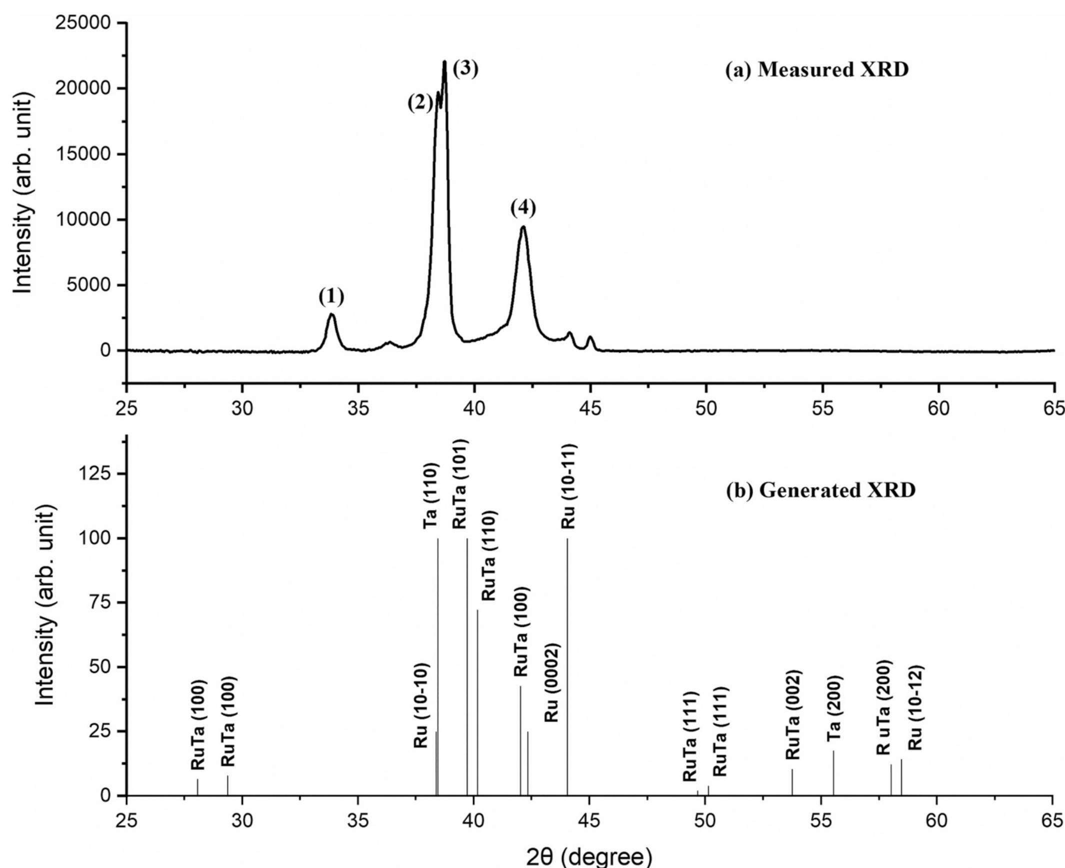

Fig. 9. (a) XRD spectrum of the Ru/Ta bilayer stack as deposited (b) XRD peaks (powdered) generated using an online app by Materials Project [43]. Crystal structures taken for reference are hexagonal Ru [46] and Cubic Ta [47] that has wide occurrence. Additionally, tetragonal [48] and cubic crystal [49] structures for RuTa composite have also been considered.

Table 6
Peak fitting parameters and crystallite size.

	Peak Position (2θ in degrees)	FWHM (2θ in degrees)	Crystallite size nm
Peak 3 (Ta (110))	38.718	0.253 ± 0.005	34.8 ± 0.7
Peak 2 (Ru (10-10)	38.436	0.549 ± 0.005	16.0 ± 0.2
Peak 4 (Ru (0002)	42.075	0.72 ± 0.01	12.4 ± 0.2

the interface have not been considered. The roughness at the surface and the interface is expected to cause scattering of the light and hinder the imaging metrics. The roughness values of thin films depend on various parameters such as processing methodology, deposition temperature, and also on co-sputtered species, if employed to enhance the morphology of thin films. [59–62] Thus, the surface roughness of a thin film manufactured using a particular technique may not accurately reflect the actual surface roughness on a mask.

3.5.2. Threshold to size (TtS), absorber reflectivity and mask bias estimation

Now that the mask models are defined, we estimate the TtS and mask bias required to evaluate our important imaging metrics using simulations. The simulation targets horizontal LnS patterns. The illumination source shape used for this simulation exercise is an IHLDP, as explained in section 2.5. The source is optimized to print at the wafer level's smallest pitch of 20 nm. The absorber stacks under consideration are a Ta-based absorber with 60 nm thickness as the reference absorber and two Ru/Ta bilayer stacks, an ideal profile, and an experimental profile corresponding to the second destructive interference, having a total absorber thickness of 53.3 nm. In order to achieve the wafer level target of 10 nm trenches with a 20 nm pitch, we must first select the mask bias that results in the highest NILS for each absorber type. The TtS corresponding to the selected mask bias was extracted and anchored for the through-pitch evaluation. As stated earlier, a dark field type of mask has been assumed for this simulation exercise.

In Fig. 12, we compare the TtS for the reference absorber, the Ru/Ta bilayer ideal case, and the Ru/Ta bilayer experimental absorber profile. The ideal Ru/Ta bilayer exhibits a slight improvement in TtS in comparison to the reference Ta-based absorber. An even higher TtS is achieved when non-idealities are considered. This is favorable as a higher TtS value translates to a lower exposure dose, and, thus, higher throughput. Two effects may explain the improvement. First, the total absorber reflectivity has deviated due to the additional layers considered in the experimental profile. A higher reflectivity of the EUV mask helps reduce the exposure dose, which in turn implies higher TtS [63]. The total absorber reflectivity with multilayer beneath for different absorber stacks has been compared in Fig. 12 (b) (the reflectivity is calculated at the centre between two adjacent mask trenches). The experimental profile results in increased reflectivity, which supports our observation. The second effect that can be used to explain the gain in TtS is the side wall angle profile. Melvin III et al. [64] refer to the absorber side wall angle of less than 90° as an open configuration. Such an open configuration allows more light into the trench, which reduces the required exposure dose [64]. In addition, Ta_2O_5 along the side wall is expected to reflect more light due to its lower k in comparison to Ta. Although the ideal profile has a lower reflectivity than the reference absorber, the slight improvement in TtS can be attributed to the wider trench observed in the bias calculation, discussed in the following paragraph.

The mask bias required for larger pitches that prints wafer level

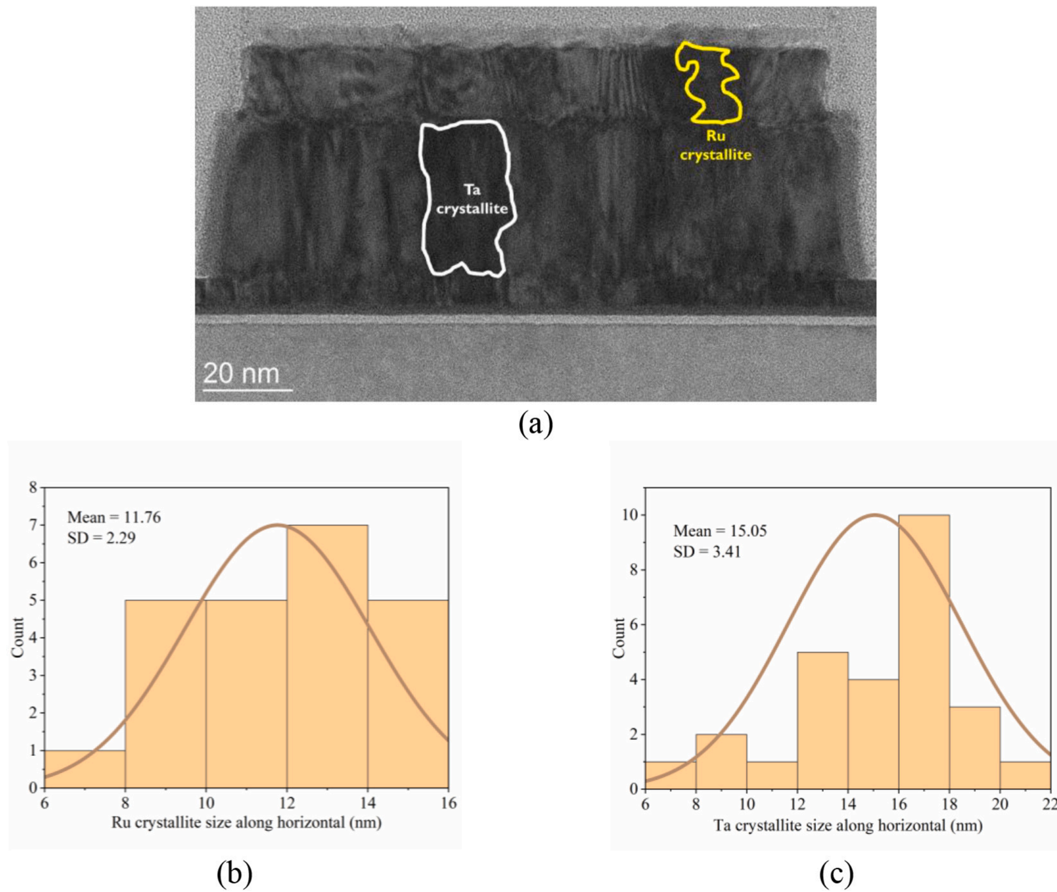

Fig. 10. (a) HR-TEM cross-section view of a patterned bilayer stack with 15.5 nm of Ru on top of 38 nm of Ta at the bottom. Crystallite identified in each layer has been highlighted for visualization. Crystallite measurements in TEM images are represented in a histogram. The mean crystallite size and the standard deviation (SD) with normalized distribution are highlighted for (b) Ru and (c) Ta layer.

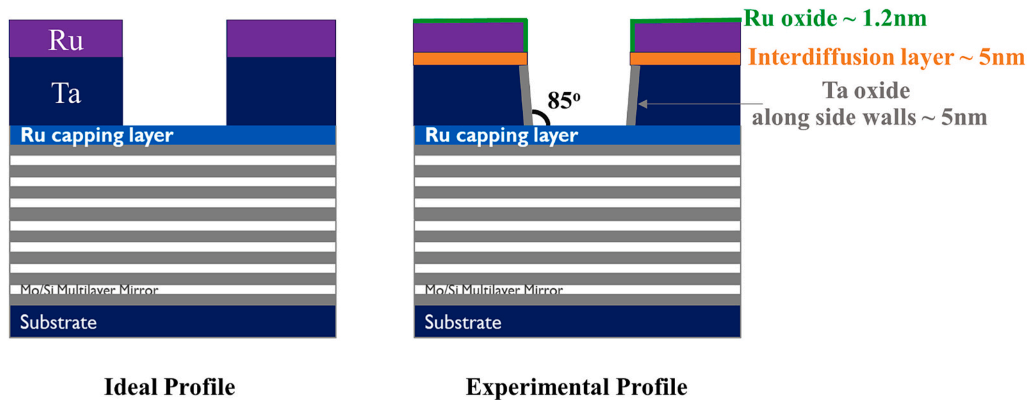

Fig. 11. Schematic representation of the two Ru/Ta bilayer stack models used for imaging simulations. The Mo/Si multilayer mirror shown is not to the scale but is just used for schematic depiction.

Table 7
Optical constants used for the additional layers in the experimental profile of the Ru/Ta bilayer absorber stack.

Layer	*n*	*k*
RuTa alloy (interdiffusion) [5]	0.927	0.025
Ta Oxide (Ta_2O_5) [14]	0.955	0.026
Ru Oxide (RuO_2) [14]	0.921	0.022

target of 10 nm trench is then computed using the respective anchored TtS for each absorber stack. The mask bias is calculated as the delta of mask trench CD minus target CD. A negative mask bias indicates that the mask trench CD needs to be smaller than the target CD. All dimensions mentioned here are taken from a wafer-level perspective. The resultant bias values are a consequence of the high NA 0.55 tool settings, illumination source shape, and the optical properties of absorber material in addition to its geometry [63,65]. We notice that the Ru/Ta bilayer absorber has more open bias than the Ta-based absorber (Fig. 13). A more open bias results in higher TtS, or lower dose-to-size, when

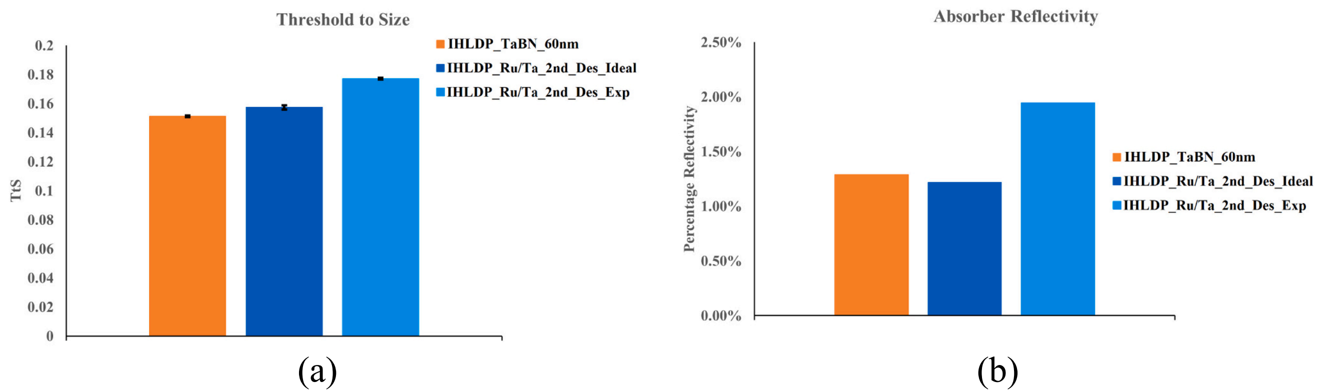

Fig. 12. A comparison of metrics between the reference Ta-based absorber and Ru/Ta bilayer stacks corresponding to second destructive interference using IHLDP illumination source optimized to pitch of 20 nm of horizontal LnS pattern (a) Threshold to Size, (corresponding to mask bias in Fig. 13) (b) total absorber reflectivity expressed in percentage, taking into account a multilayer below.

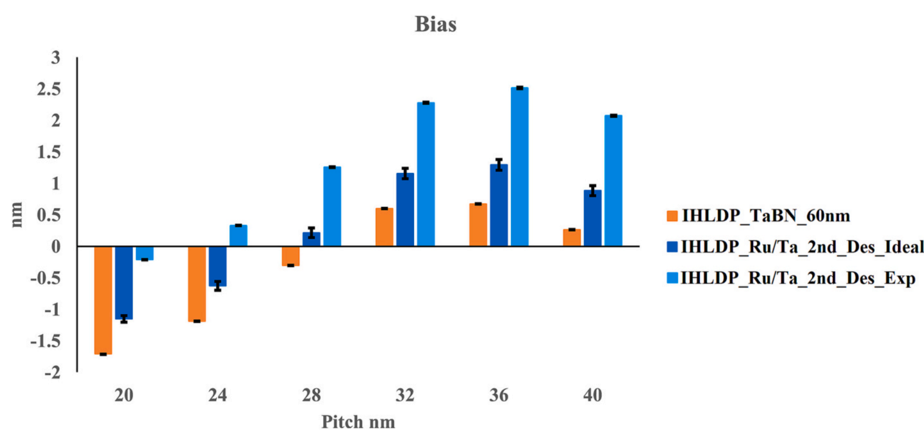

Fig. 13. Bias calculated for each absorber using respective TtS anchored to the smallest pitch of 20 nm using an IHLDP illumination source. Absorbers under consideration include reference Ta-based absorber and Ru/Ta bilayer stacks corresponding to second destructive interference.

compared to Ta-based. This is a general trend seen for low-*n* absorber materials, and these findings are consistent with that of van Lare et al. for NA 0.33 [63]. This justifies the minor improvement in TtS for Ru/Ta ideal stack in comparison to Ta-based absorber, even when the reflectivity is slightly lower.

Furthermore, considering the 3D mask structure, the absorber SWA will also have an impact on the diffraction order intensities, which in turn is expected to affect the bias and TtS; this discussion goes beyond the scope of this paper. Since many factors, such as the absorber's optical properties, thickness and geometry, illumination source shape, anamorphic imaging, and central obscuration, simultaneously play their role, it is a bit challenging to disentangle the effects from each cause and quantify them. Therefore, the mask bias is quite case-specific and largely depends on the balancing of the diffraction orders to achieve an optimum image quality.

Now that the TtS and bias have been fixed for each absorber case, we can proceed to evaluate the imaging metrics discussed in the following sub-sections.

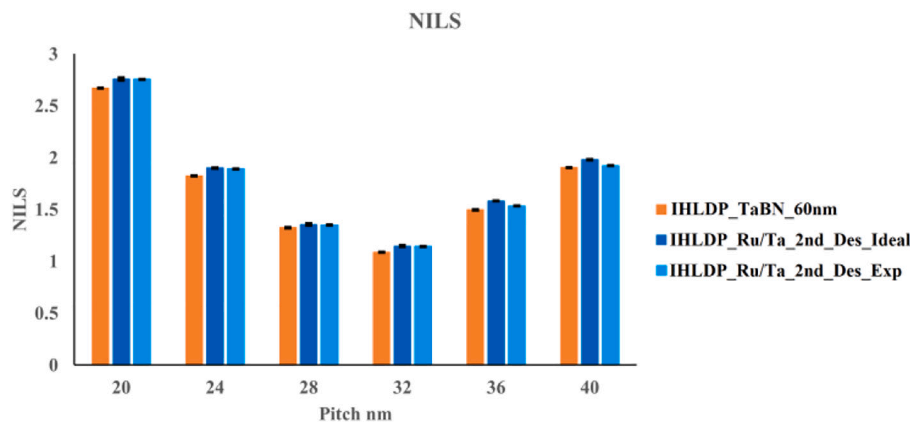

Fig. 14. Through-pitch comparison of NILS, evaluated at respective TtS anchored to the smallest pitch of 20 nm for each absorber using IHLDP illumination source.

3.5.3. NILS

A through-pitch behavior of NILS is compared for the three absorber stacks under Study in Fig. 14. As it can be seen, the two bilayer stacks exhibit improved NILS through pitch compared to the reference TaBN absorber. This improvement in NILS can be attributed to the bilayer stacks having a lower overall *n* than TaBN. The decline in NILS for larger pitches can be attributed to two key factors discussed in the following paragraphs.

Firstly, the illumination source has been optimized to our smallest target pitch of 20 nm. In a through-pitch exercise, this is unlikely to produce the best NILS for the other pitches, and trade-offs are expected even if the illumination source is optimized to any other pitch.

Secondly, as a high NA 0.55 EUV lithography tool employs a central obscuration in the projection optics, some parts of the higher diffraction orders get blocked. In comparison to when there is no central obscuration, NILS decreases for bigger pitches whose higher diffraction orders lie in the obscuration region. Coming back to our discussion of LnS patterns, for pitch 20 nm to 28 nm, only two diffraction orders are captured, and they do not lie in the obscuration region. Therefore, the interference of only these two diffraction orders governs the outcome that depends on their respective amplitudes and the phase relationship between them. At a pitch of 32 nm, some parts of the +/−first diffraction orders fall in the obscuration area. Although a very minor part of the second-order diffraction orders is captured, it does not improve the NILS. As a result, we observe the lowest point in NILS at a pitch of 32 nm. As pitch increases from 36 nm to 40 nm, more diffraction orders are captured, which justifies the upward trend in NILS.

A slight deviation in NILS for the experimental profile can be attributed to several factors. To begin with, we must acknowledge that the NILS is evaluated at different values of TtS and focus for the Ru/Ta bilayer ideal profile and the experimental profile. NILS and TtS often exhibit trade-offs; therefore, a slight reduction in NILS can be easily justified with a higher TtS of the experimental profile against the ideal. This reduction in NILS can be explained by simplifying the NILS formula in Eq. 2 [66]. The inverse relationship between the NILS and the TtS at which it is evaluated is apparent.

$$NILS = CD\,\frac{1}{TtS}\,\frac{dI}{dx} \tag{2}$$

Where *CD* is the Critical Dimension, *dI/dx* is the slope of the image intensity as of function of position, and *TtS* is the intensity at which it is normalized [66].

To have a better understanding, we must also compare the aerial images formed at the best focus position on the wafer in these two cases (Fig. 15). It can be noticed that the experimental profile shows a rise in the peak intensity in comparison to the ideal profile, which is an advantage. This indicates a higher number of photons in the central region, which should help in preventing the blockage in the developer path of resist, leading to lower defectivity. [67] However, the intensity in the tail region is also slightly uplifted. Both of these observations are a consequence of increased reflectivity in the case of the experimental profile. Although the image contrast and the image slope in the experimental profile exhibit a minor increment, the increased intensity (TtS) in the denominator term of Eq. 2 suppresses the gain. As a result, we see a minor drop in the NILS, as explained before.

Another viewpoint to look at this scenario is from the absorber SWA perspective. Melvin III et al. [64] point out in their study that, because of the geometry of the absorber, the optical path for light traveling through an open absorber configuration is shorter. This optical path reduction is also observed by the light reflected internally within the absorber. The number of these pathways increases as the SWA decreases, allowing light to leak and ultimately reducing the contrast (NILS) [64]. In the case of our experimental absorber profile, the Ta-oxide along the tilted side wall is less absorptive due to its lower *k* in comparison to Ta, resulting in a leaky absorber.

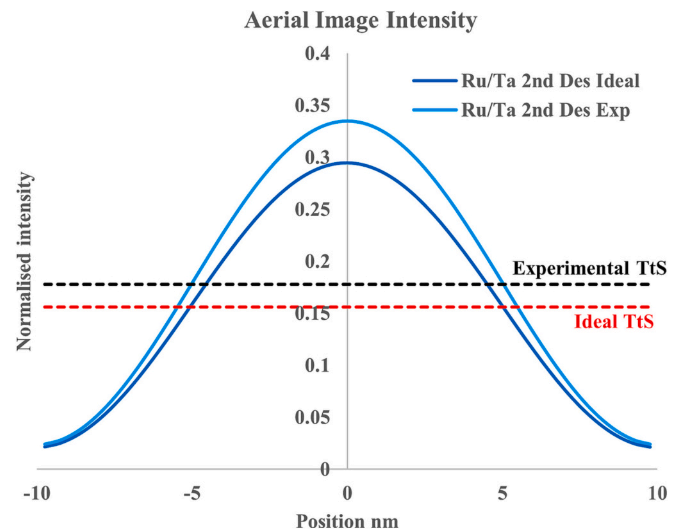

Fig. 15. Aerial image intensity distribution of horizontal LnS at the wafer level for the Ru/Ta bilayer stack. The intensities of the ideal and experimental absorber profiles are compared for the smallest pitch of 20 nm with a target of 10 nm using the IHLDP illumination source.

3.5.4. TCE

The next imaging metric we will discuss is telecentricity error. The through-pitch behavior of TCE is compared in Fig. 16. The TCE values in the bar graphs that are being compared represent the modulus values. NILS and TCE often exhibit trade-offs as a function of the optical properties of absorber materials, which is also evident in our results. Moreover, TCE also depends on the pitch under consideration, mask bias, and illumination source (including the angle of incidence and position of the poles in an illumination source). Since we prioritized a higher NILS while optimizing the mask bias, the reported TCE values are its consequence. In addition to the off-axis illumination used in EUV lithography, TCE is caused by an imbalance in intensity between the diffracted orders [15]. This imbalance in the intensity is a consequence of mask apodization, the absorber's optical properties, and the shadowing effect caused by the absorber's thickness [15]. Therefore, to have a deeper insight, we must examine a 2D (two-dimensional) pupil map of diffracted order intensities.

A comparison between 2D pupil maps of diffracted order intensities for the Ru/Ta bilayer ideal profile and the experimental profile is made in Fig. 17. The figure illustrates two 0th-order poles corresponding to the inner half leaf-shaped dipole with their respective 1st diffraction orders. Only one pole of either −1 or + 1 diffraction order is captured. The central region shaded in black represents the obscuration area. The imbalance between the intensity distribution of the diffracted orders of the experimental profile and the ideal profile is evident from the images. This observation validates the increased TCE at the pitch of 20 nm for the experimental Ru/Ta absorber profile. A similar analysis could also be made for other pitches. SMO (Source Mask Optimization) techniques could be employed to further reduce the TCE. The imbalance in the diffraction orders may be compensated by adopting non-uniform dipole illumination.

3.5.5. BFV

Turning now to best focus variation through pitch, the difference between the maximum and the minimum best focus values for the pitches under consideration is depicted in Fig. 18. Ru/Ta bilayer stacks, even with the non-idealities, exhibit reduced BFV for the inner half leaf-shaped illumination source, which proves to be an advantage [68].

A simple explanation to justify the reduced BFV is that the effective *k* (0.033995) of the Ru/Ta bilayer (ideal profile) is slightly higher than the bulk of the reference TaBN absorber (0.0307). The high *k* mask absorber

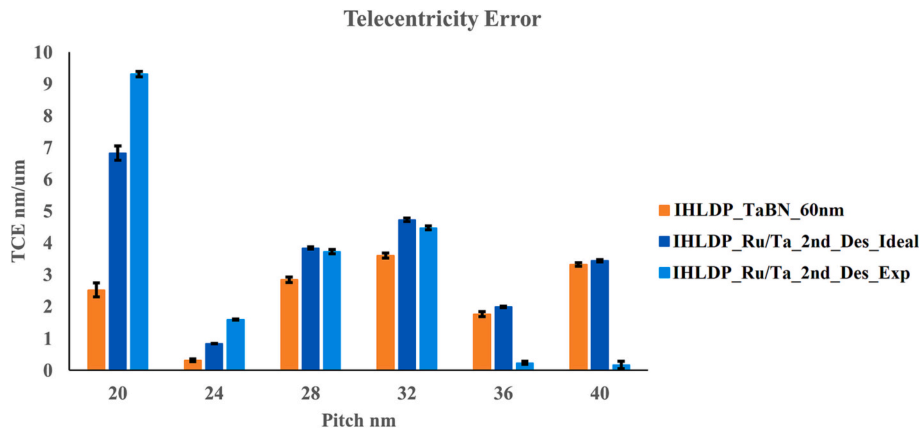

Fig. 16. Through-pitch comparison of telecentricity error, evaluated at respective TtS anchored to the smallest pitch of 20 nm for each absorber using IHLDP illumination source.

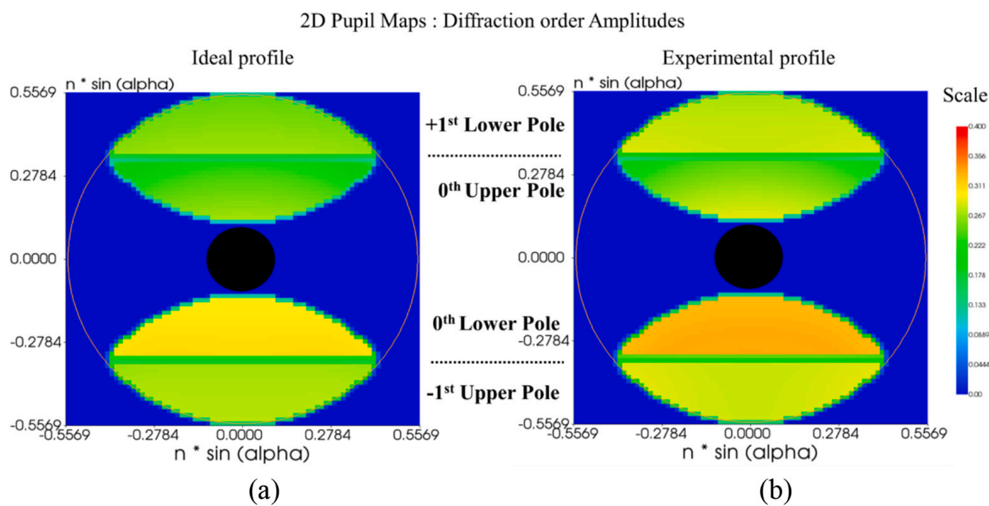

Fig. 17. 2D pupil maps of diffracted order intensities represented with a colored scale on the right at high NA 0.55 for LnS patterns having a pitch 20 nm using IHLDP illumination source (a) ideal Ru/Ta profile, (b) experimental Ru/Ta profile. The black circle in the center of each pupil map indicates obscuration.

Fig. 18. Comparison of best focus variations through pitch for each absorber stack using IHLDP illumination source. Displayed values correspond to the difference between the maximum and the minimum best focus values for the pitches under consideration.

simulation study supports the anticipated reduction in BFV. [28,69] The increased BFV in the case of the experimental profile can be attributed to reduced k at the side walls due to a Ta-oxide layer formation.

Another aspect that has been mentioned in the literature is that, at the interface of the vacuum and the absorber, a mismatch in refraction coefficient n results in phase distortion, which in turn causes BFV [28,70]. Contradictory, although this mismatch of n in the case of an experimental profile is less in comparison to the ideal profile, the difference is not strong enough to observe a reduction in BFV. On the other hand, it appears that the lower k of Ta-oxide at the side wall is sufficient

enough reason to observe an increment in BFV, as stated in the previous paragraph. This point must be interpreted cautiously because the mask bias and the SWA effect have not been considered due to complexity.

Going further, it encourages research into the phase of the diffraction orders, as suggested in the literature. Simulation studies have pointed out the nonlinear relationship between the best focus and the absorber's n and k [71,72]. Results presented by Finders et al. [71] and Mesilhy et al. [72] show that the best focus behavior of materials with n between 1 and 0.92 differs from those with n between 0.92 and 0.88 for absorber thickness of 40 nm. As previously mentioned, the computed average n value for an ideal Ru/Ta bilayer stack is around 0.926, placing our absorber stack at the transition point. Mesilhy H. et al. [72] have observed that for a fixed absorber thickness of 40 nm, materials with $1 < n < 0.92$ show a positive best focus shift, whereas materials with $0.92 < n < 0.88$ exhibits a negative best focus shift. Although the results presented by the author are for a fixed absorber thickness to print a space target ranging from 8 nm to 20 nm having a pitch five times the target, we must acknowledge that the absorber will exhibit a transition in the best focus trend of the spaces, which indicates nonlinear behavior. Finders et al. [71] have expressed similar behavior in terms of the zeroth order phase offset of the diffraction orders and recommend reducing the zeroth order phase discontinuity in order to reduce the best focus shifts. Therefore, we aim to examine the zeroth order phase discontinuity of the absorbers under consideration to understand their best focus behavior. Before examining the zeroth order phase discontinuity, it is essential to know the pitches that contribute to the BFV. Fig. 19 displays the best focus values of each pitch for different absorber stacks. We can see that pitch 24 nm and 32 nm determines the BFV due to their extremities. It is worth noting that the polarity of best focus at pitch 32 nm is flipped for the Ta-based absorber, and the bilayer stacks exhibit maximum deviation; therefore, it is interesting to investigate this pitch. It is also important to remember that a small part of the diffraction orders resides in the obscuration region for pitch 32 nm, and a very tiny part of the second order is captured. The most practical solution for understanding how both factors affect the best focus value is to observe simulation results, as a simple two-plane waves interference equation cannot describe it.

Returning to the topic of the zeroth order phase discontinuity, the absorber stacks are compared in terms of the relative phase difference between the diffraction orders with respect to the zeroth diffraction order at pitch 32 nm (Fig. 20). The phase of diffraction orders is evaluated at the mask sigma setting of the s-litho software, corresponding to the smallest pitch's telecentric sigma. A second-order polynomial fitting is used to plot the dotted trendline to highlight the zeroth-order discontinuity. The zeroth order discontinuity is much more in the case of Ta-based when compared to bilayer stacks, resulting in a larger BFV. The experimental profile exhibits slightly more zeroth-order phase discontinuity than the ideal profile, which justifies the increased BFV.

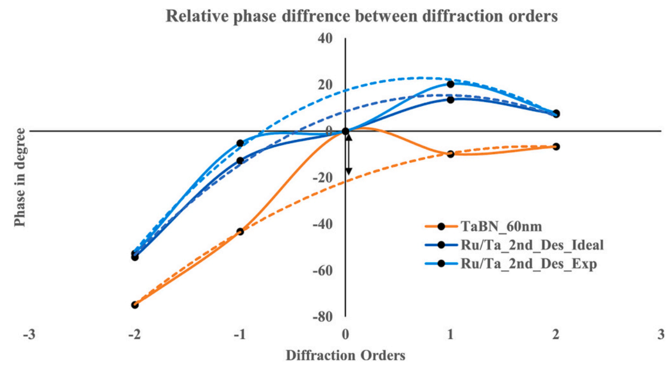

Fig. 20. Phase across the diffraction orders of horizontal LnS patterns targeting 10 nm space with 32 nm pitch at wafer level for absorbers under consideration. The phase of diffraction orders is evaluated at the mask sigma setting of the s-litho software, corresponding to the smallest pitch's telecentric sigma. A second-order polynomial fitting is used to plot the dotted trendline to highlight the zeroth-order discontinuity.

However, these results should be cautiously interpreted, and their generalization is not encouraged. As stated earlier, BFV also depends on the shape of the illumination source, and the chosen bias will have an influence on the phase of diffraction orders. Therefore, a holistic overview is necessary to comprehend BFV behavior. In our previous research, we observed that an IHLDP (small sigma) illumination source demonstrated a larger BFV than other illumination source types for the reference Ta-based and TaCo alloy absorbers [20]. Burkhardt et al. [73] have reported similar observations using an inner/a small sigma illumination source for the investigated absorbers. Acknowledging the factors that impact BFV, it becomes challenging to predict the overall trend in the outcome without rigorous simulations. Therefore, it is highly recommended to compare the imaging performance of any given absorber at a particular thickness, using different illumination source shapes for a better understanding. The observations made in this study are only valid for horizontal LnS. According to A. Erdmann et al. [74], the vertical LnS are more susceptible to M3D effects than horizontal features due to orientation-dependent mask scaling in high NA systems. Therefore trends in imaging metrics for vertical LnS must be addressed separately in addition to the illumination source shape for Ru/Ta bilayer absorber stack, which is planned in our subsequent research paper.

3.5.6. *Contribution of individual mask non-idealities*

In this sub-section, we discuss the simulation results obtained using only one non-ideality at a time, viz. the Sidewall Angle, Ta oxide along the sidewall, Ru oxide at the top, and interdiffusion at the bilayer interface. The percentage deviation observed in imaging metric values

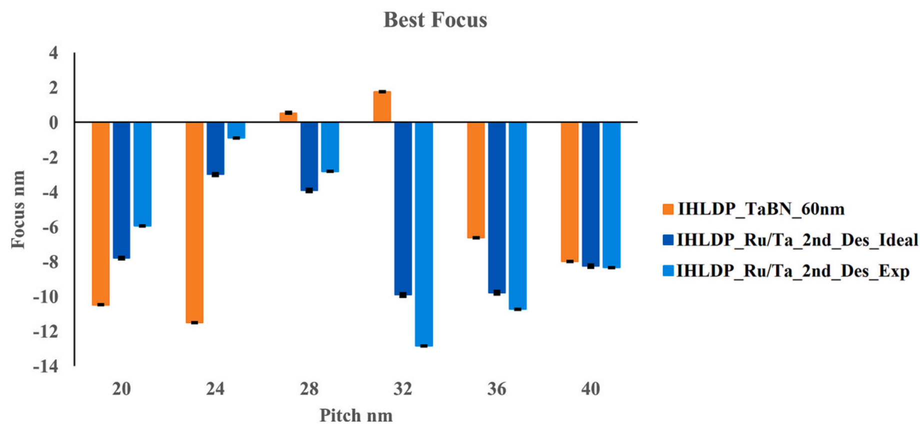

Fig. 19. Through-pitch comparison of best focus values of each pitch for different absorbers.

compared to the ideal Ru/Ta bilayer absorber stack for the smallest pitch is tabulated as shown in Fig. 21. Let us examine the contribution of each non-ideality individually.

Starting with the NILS, we observe that the SWA favors improvement in NILS. Although Ta oxide along the sidewall and Ru oxide at the top are responsible for NILS reduction, the overall effect of all non-idealities in consideration demonstrates improvement. The major contributor to TtS improvement in the experimental profile happens to be the Ru oxide at the top, supposedly due to increased reflectivity.

Moving onto to TCE as the next non-ideality, it appears that Ru oxide at the top and interdiffusion at the bilayer interface play a significant role in the increment observed for the experimental stack. Lastly, the increased BFV in the experimental profile can be majorly attributed to the interdiffusion layer at the bilayer interface.

The outcome suggests that the interdiffusion at the bilayer interface must be kept in control. Therefore, an in-depth investigation is suggested to regulate the interdiffusion utilizing various deposition processes and its parameters.

3.5.7. *Phase shift*

In addition, it is also worthwhile to compare the phase shift induced by each absorber (Fig. 22). A phase shift of 200° to 230° is considered to be optimum for an attenuated Phase Shift Mask (PSM) candidate [75]. Moreover, the total absorber reflectivity (Fig. 12 b) for Ru/Ta bilayer stacks, including the ML mirror, is ≤ 2%, which was the specification limit set by Luong et al. [28] for Ni-based high-k absorbers. A lower reflectivity is expected to reduce the side lobe printing problem faced by most of the PSM absorbers presented in the literature [74], which have a reflectivity >6%. Besides that, Ru/Ta bilayer stacks do not show reduced TtS, unlike high-k absorbers. Overall, Ru/Ta bilayer stacks, which marginally match the phase shift and reflectivity recommendations, have been found to mitigate M3D effects moderately.

3.5.8. *Effect of n, k, and thickness variations*

Next, we study the effect of n, k, and thickness variations. As mentioned in the methodology Sec 2.5, we have limited our simulation exercise to an LDP type of illumination and 10 nm wafer level target CD having a 20 nm pitch. We have considered nine unique combinations of Ta-based absorber and eighty-one unique combinations of Ru/Ta bilayer absorber stack corresponding to 2nd destructive interference having 15.3 nm of Ru on top of 38 nm of Ta layer. The mean and error values of imaging metrics assuming normal distribution have been listed in Table 8.

We observe the error to be small enough to demonstrate confidence in our simulation results. As a result, we can infer that a ± 2% deviation in optical parameters and ± 0.5 nm thickness variation in the absorber stack won't significantly affect the NILS and TtS whereas TCE is expected to vary marginally.

4. Summary & conclusion

Low-n mask absorbers are being researched actively by the industry as potential mitigation of image contrast fading and M3D imaging effects in EUV lithography. Ru is a typical material with low-n optical EUV properties, but as it is also used as the capping layer on the Mo/Si multilayer mirror, alloys with Ru are challenging to pattern selectively to the Ru cap. With a bilayer absorber approach using Ru and Ta, the patterning challenge can be easily solved, which is possible because of the excellent etch selectivity between Ru and Ta layers demonstrated by Cl_2-O_2 and Cl_2-N_2 RIE. Moreover, a bilayer approach increases the degree of freedom by allowing the optical properties to be tuned through thickness adjustments, which are not restricted by the stable composition of an alloy, as in the case of single-layer absorbers. In addition, the swing in the imaging metrics as a function of absorber thickness can be controlled using the thin film interference phenomenon, either by constructive or destructive interference between the light reflected from the top of the absorber and the bilayer interface. Of course, these additional benefits come at the expense of extra steps required during repair and etch. The crystallinity of an absorber material is expected to have a small impact on the imaging metrics; therefore, different deposition methodologies must be explored to regulate the crystallinity. To account for the non-idealities in material and geometry, data obtained from the experimental characterization of the patterned bilayer was used to model the absorber stack employed for imaging simulations. When compared to the Ta-based absorber, the lower average *n* of the bilayer stack is responsible for the overall NILS improvement. This results from Ru's inherent optical characteristics (low *n* & low *k*), which also explains improved TtS and NILS. Ru/Ta bilayer exhibits increased TCE due to an imbalance between the intensity distribution of the diffracted orders revealed by 2-D pupil maps. With selected bias and inner half leaf dipole illumination, the Ru/Ta bilayer shows a reduction in BFV. We know that the imaging metrics also depend on the shape of the illumination source shape; therefore, it would be interesting to examine how these metrics behave using other source shapes such as full leaf

Contribution \ Metrics	NILS	TtS	TCE	BFV
Ideal Profile	2.7222	0.1560	6.5414	7.7795
Experimental Profile	0.20%	14.07%	41.10%	43.51%
Sidewall Angle	0.17%	-0.95%	1.30%	-37.36%
Ta Oxide along Sidewall	-0.16%	3.67%	0.95%	7.92%
Ru Oxide at the top	-0.21%	34.20%	37.19%	0.66%
Interdiffusion at Bilayer interface	0.07%	5.82%	40.83%	55.03%

Good — Moderate — Poor

Fig. 21. Percentage deviation observed in imaging metrics compared to ideal Ru/Ta bilayer absorber stack for the smallest pitch. A negative value indicates reduction, whereas a positive value indicates an increment in the corresponding value of that parameter with respect to the ideal profile. The relative color scheme signifies the change in the attributes as good moderate, and poor.

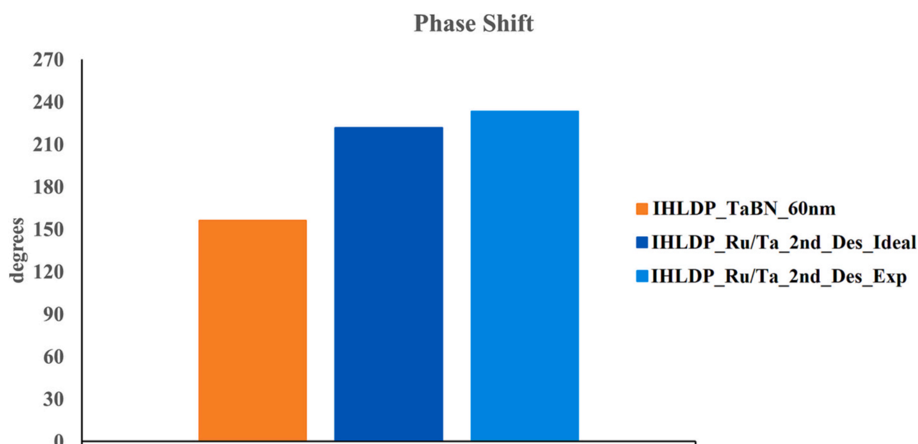

Fig. 22. Phase shift induced by different absorbers stacks.

Table 8
Mean and standard error values of imaging metrics considering n, k, and thickness variations.

Absorber Stack\Imaging metrics	NILS	TCE	TtS	Bias
TaBN				
Mean	2.46	8.4	0.163	−1.3
±Error	0.06	0.6	0.003	0.1
Ru/Ta_2nd Des				
Mean	2.61	10.8	0.153	−1.21
±Error	0.01	0.2	0.002	0.06

dipole and outer half leaf dipole. Although the impact of SWA is not discussed in detail in this study, a small change of 5° from the ideal 90° profile is expected to adversely affect the imaging metrics depending on the orientation of the LnS pattern [76]. The 85° SWA with other non-idealities in the Ru/Ta bilayer experimental absorber profile has demonstrated some deviation in the imaging metrics from the ideal profile. The contribution of individual non-idealities study suggests regulating the interdiffuion at the bilayer interface either by improving existing deposition processes or by investigating alternative deposition techniques that have the potential to do so. Even when non-idealities are considered, the simulation findings demonstrate that the Ru/Ta bilayer absorber exhibits improved NILS and reduced BFV compared to the Ta-based absorber. The NILS and TtS won't be severely impacted by a ± 2% deviation in optical parameters and a ± 0.5 nm thickness variation in the absorber stack, however TCE is anticipated to be marginally affected. Finally, the outcome of this study encourages further research into the possibilities of multilayer absorbers, where the optical characteristics can be tailored by varying the thickness of individual layers.

Declaration of Competing Interest

The authors declare that they have no known competing financial interests or personal relationships that could have appeared to influence the work reported in this paper.

Data availability

Data will be made available on request.

Acknowledgments

The authors would kindly like to thank imec's Material and Characterization (MCA) team, Sofie Mertens (imec) for helping with depositions, Patrick Jaenen (imec) and Joost Bekaert (imec) for DUV lithography, Stefan Decoster (imec) and Laurent Souriau (imec) for discussions regarding etch process, Farid Sebaai (imec) for hard mask removal, Dennis Van Dorp (imec) for assistance during the lab experiments, Olivier Richard (imec) for TEM discussions, Pratik Bagul (KU Leuven, imec) and Hilde Tielens (imec) for XRD discussion, Qais Saadeh (PTB) and Nick Pellens (imec) for insights on optical constants and thickness variations.

Appendix A. EDS-STEM of a bilayer etch with the hard mask still present for 2nd destructive absorber stack with 15.5 nm of Ru on top of 38 nm of Ta etched with two steps etch process, distinct X-ray emissions with unique attributes can be identified by the color

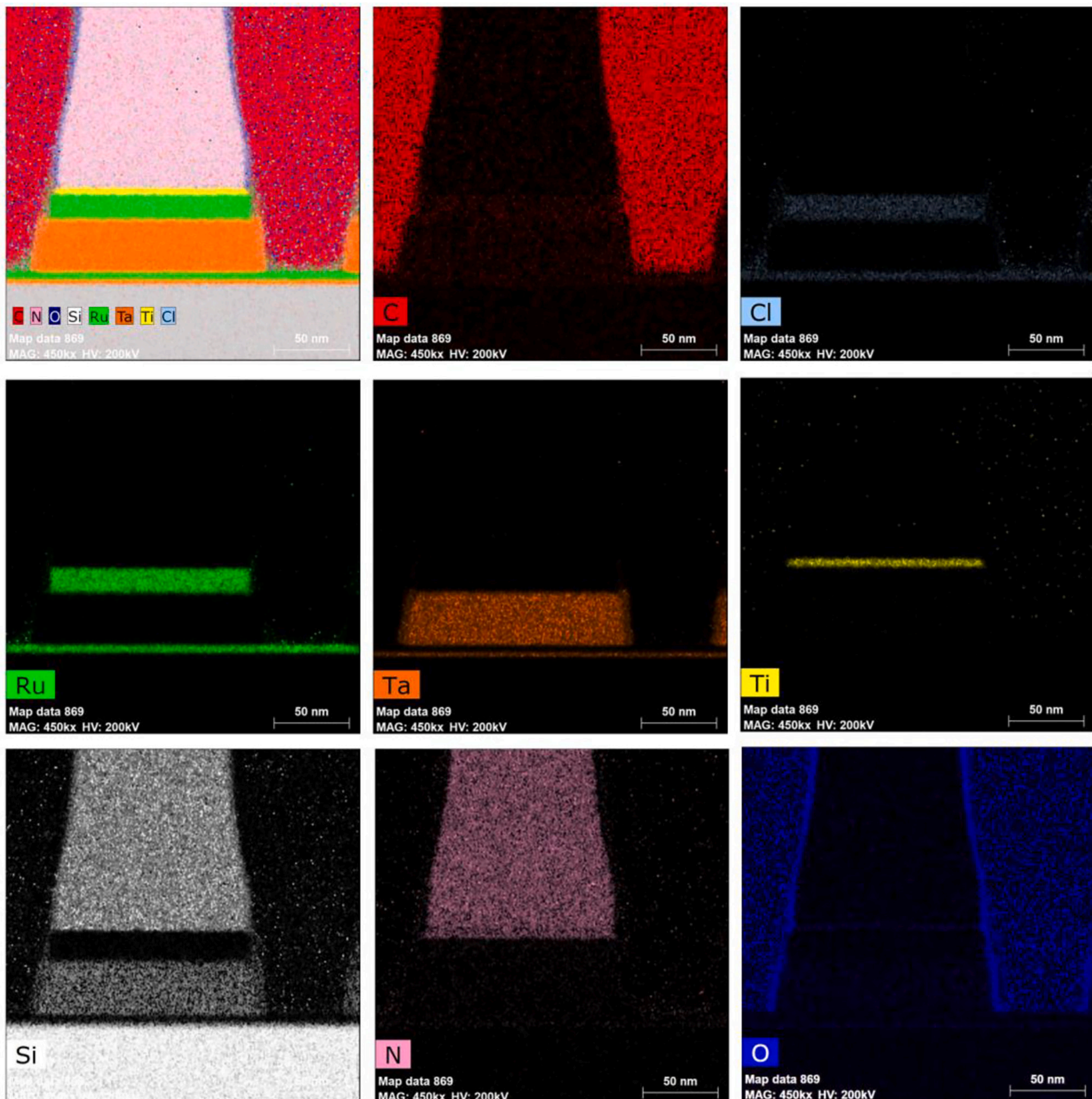

References

[1] A. Erdmann, et al., Characterization and mitigation of 3D mask effects in extreme ultraviolet lithography, Adv. Opt. Technol. 6 (3–4) (2017) 187–201, https://doi.org/10.1515/aot-2017-0019.

[2] V. Philipsen et al., "Reducing extreme ultraviolet mask three-dimensional effects by alternative metal absorbers," J. Micro. Nanolithogr. MEMS MOEMS 16(4), 041002 doi: https://doi.org/10.1117/1.JMM.16.4.041002.

[3] A. Erdmann, et al., Attenuated phase shift mask for extreme ultraviolet: can they mitigate three-dimensional mask effects? J. Micro. Nanolithogr. MEMS MOEMS 18 (01) (2018) 1, https://doi.org/10.1117/1.JMM.18.1.011005.

[4] C. van Lare, F.J. Timmermans, J. Finders, Alternative reticles for low-k1 EUV imaging, in: K.G. Ronse, et al. (Eds.), International Conference on Extreme Ultraviolet Lithography 2019, SPIE, 2019, https://doi.org/10.1117/12.2536415.

[5] M. Wu, et al., Characterization of Ru4-xTax (x = 1,2,3) alloy as material candidate for EUV low-n mask, Micro Nano Eng. 12 (100089) (2021), 100089, https://doi.org/10.1016/j.mne.2021.100089.

[6] J. Van Schoot, et al., High-NA EUV lithography exposure tool: Advantages and program progress, in: K.G. Ronse, et al. (Eds.), Extreme Ultraviolet Lithography 2020, SPIE, 2021, https://doi.org/10.1117/12.2572932.

[7] Y. Ikebe, O. Nozawa, T. Onoue, Development of high reflective phase shift type absorber for future generation EUV mask blank (conference Presentation), in: N. M. Felix, A. Lio (Eds.), Extreme Ultraviolet (EUV) Lithography XI, SPIE, 2020, https://doi.org/10.1117/12.2550941.

[8] H.M.S. Mesilhy, et al., Pathfinding the perfect EUV mask: Understanding the EUV mask using the hybrid mask model, in: K.G. Ronse, et al. (Eds.), International Conference on Extreme Ultraviolet Lithography 2021, SPIE, 2021, https://doi.org/10.1117/12.2601243.

[9] Pei-yang Yan, et al., Extreme ultraviolet–embedded phase-shift mask, J. Micro. Nanolithogr. MEMS MOEMS 10 (3) (2011), 033011, https://doi.org/10.1117/1.3616060.
[10] I. Kang, et al., Optimal phase shift and reflectance for high numerical aperture EUV phase shift mask, in: S.P. Renwick (Ed.), Photomask Technology 2021, SPIE, 2021, https://doi.org/10.1117/12.2602035.
[11] J. Seejun, et al., Improved photon shot noise effect on LWR by using attenuated PSM for EUVL, in: International Workshop on EUV Lithography, 2013 https://www.euvlitho.com/2013/P31.pdf Accessed 8 Jan. 2023.
[12] H. Mesilhy, et al., Investigation of waveguide modes in EUV mask absorbers, J. Micro/Nanopattern. Mats. Metro. 20 (02) (2021), https://doi.org/10.1117/1.JMM.20.2.021004.
[13] S-Litho-euv, Synopsys 690 East Middlefield Road, Mountain View, CA 94043, USA https://www.synopsys.com/silicon/mask-synthesis/sentaurus-lithography.html.
[14] B.L. Henke, E.M. Gullikson, J.C. Davis, X-ray interactions: Photoabsorption, scattering, transmission, and reflection at E = 50-30,000 eV, Z = 1-92, At. Data Nucl. Data Tables 54 (2) (1993) 181–342, https://doi.org/10.1006/adnd.1993.1013.
[15] E. van Setten, et al., Edge placement error control and Mask3D effects in High-NA anamorphic EUV lithography, in: P.A. Gargini, et al. (Eds.), International Conference on Extreme Ultraviolet Lithography 2017, SPIE, 2017, https://doi.org/10.1117/12.2280624.
[16] L. de Winter, et al., High NA EUV scanner: Obscuration and wavefront description, in: K.G. Ronse, et al. (Eds.), Extreme Ultraviolet Lithography 2020, SPIE, 2020, https://doi.org/10.1117/12.2572878.
[17] I.A. Makhotkin, et al., Refined extreme ultraviolet mask stack model, J. Opt. Soc. Am. A Opt. Image Sci. Vis. 38 (4) (2021) 498, https://doi.org/10.1364/josaa.416235.
[18] J.-H. Franke, et al., Improving exposure latitudes and aligning best focus through pitch by curing M3D phase effects with controlled aberrations, in: K.G. Ronse, et al. (Eds.), International Conference on Extreme Ultraviolet Lithography 2019, SPIE, 2019, https://doi.org/10.1117/12.2537104.
[19] B. Bilski, et al., High-NA EUV imaging: Challenges and outlook, in: F. Behringer, J. Finders (Eds.), In 35th European Mask and Lithography Conference (EMLC 2019), U, SPIE, 2019, https://doi.org/10.1117/12.2536329.
[20] D. Thakare, A. Delabie, V. Philipsen, Optimizing EUV imaging metrics as a function of absorber thickness and illumination source: Simulation case study of ta-co alloy, in: U. Behringer (Ed.), In 37th European Mask and Lithography Conference, SPIE, 2022, https://doi.org/10.1117/12.2640098.
[21] D. Civay, et al., EUV telecentricity and shadowing errors impact on process margins, in: O.R. Wood, E.M. Panning (Eds.), Extreme Ultraviolet (EUV) Lithography VI, SPIE, 2015, https://doi.org/10.1117/12.2087639.
[22] G. McIntyre, et al., Modeling and experiments of non-telecentric thick mask effects for EUV lithography, in: F.M. Schellenberg, B.M. La Fontaine (Eds.), Alternative Lithographic Technologies, SPIE, 2009, https://doi.org/10.1117/12.813536.
[23] F. Grillo, et al., Area-selective deposition of ruthenium by area-dependent surface diffusion, Chem. Mater. 32 (22) (2020) 9560–9572, https://doi.org/10.1021/acs.chemmater.0c02588.
[24] M. Yamada, M. Nakaishi, K. Sugishima, An etching mechanism of ta by chlorine-based plasmas, J. Electrochem. Soc. 138 (2) (1991) 496–499, https://doi.org/10.1149/1.2085617.
[25] M.H. Shin, et al., Etching characteristics of ta and TaN using Cl2/Ar inductively coupled plasma, Thin Solid Films 506–507 (2006) 230–234, https://doi.org/10.1016/j.tsf.2005.08.019.
[26] H.W. Kim, Characteristics of Ru etching using ICP and helicon O2/Cl2 plasmas, Thin Solid Films 475 (1–2) (2005) 32–35, https://doi.org/10.1016/j.tsf.2004.07.046.
[27] S. Verhaverbeke, J.W. Parker, A model for the etching of Ti and TiN in SC-1 solutions, Mater. Res. Soc. Symp. Proc. 477 (447) (1997), https://doi.org/10.1557/PROC-477-447.
[28] V. Luong, et al., Ni-Al alloys as alternative EUV mask absorber, Appl. Sci. (Basel) 8 (4) (2018) 521, https://doi.org/10.3390/app8040521.
[29] V. Philipsen, et al., Novel EUV mask absorber evaluation in support of next-generation EUV imaging, in: J.H. Rankin, E.E. Gallagher (Eds.), Photomask Technology 2018, SPIE, 2018, https://doi.org/10.1117/12.2501799.
[30] S. Raghunathan, et al., Experimental measurements of telecentricity errors in high-numerical-aperture extreme ultraviolet mask images, J. Vac. Sci. Technol. B Nanotechnol. Microelectron. 32 (6) (2014) 06F801, https://doi.org/10.1116/1.4901876.
[31] Y. Chen, et al., Tip-to-tip variation mitigation in extreme ultraviolet lithography for 7 nm and beyond metallization layers and design rule analysis, J. Vac. Sci. Technol. B Nanotechnol. Microelectron. 35 (6) (2017) 06G601, https://doi.org/10.1116/1.4994908.
[32] C. Zahlten, et al., High-NA EUV lithography: pushing the limits, in: 35th European Mask and Lithography Conference (EMLC 2019), U. F. Behringer and J. Finders, Eds, SPIE, 2019, https://doi.org/10.1117/12.2536469.
[33] N.V. Davydova, et al., Fundamental understanding and experimental verification of bright versus dark field imaging, in: K.G. Ronse, et al. (Eds.), Extreme Ultraviolet Lithography 2020, SPIE, 2020, https://doi.org/10.1117/12.2573161.
[34] Q. Saadeh, et al., Time-frequency analysis assisted determination of ruthenium optical constants in the sub-EUV spectral range 8 nm – 23.75 nm, Opt. Express 29 (25) (2021) 40993.
[35] Q. Saadeh, et al., Nested sampling aided determination of tantalum optical constants in the EUV spectral range, Appl. Opt. 61 (33) (2022) 10032–10042.
[36] C.C. Hsu, J.W. Coburn, D.B. Graves, Etching of ruthenium coatings in O2- and Cl2-containing plasmas, J. Vac. Sci. Technol. A 24 (1) (2006) 1–8, https://doi.org/10.1116/1.2121751.
[37] T. Brückl, H. Zull, Actinometry of inductively coupled Cl2/N2 plasmas for dry etching of GaAs, J. Appl. Phys. 98 (2) (2005), 023307, https://doi.org/10.1063/1.1994932.
[38] K.P. Lee, et al., Comparison of plasma chemistries for dry etching of Ta2O5, J. Vac. Sci. Technol. A 18 (4) (2000) 1169–1172, https://doi.org/10.1116/1.582319.
[39] M. Knotter, D. Dee Denteneer, Etching mechanism of silicon nitride in HF-based solutions, J. Electrochem. Soc. 148 (3) (2001), https://doi.org/10.1149/1.1348262.
[40] J.A. Bearden, A.F. Burr, Reevaluation of X-ray atomic energy levels, Rev. Mod. Phys. 39 (1) (1967) 125–142. https://journals.aps.org/rmp/pdf/10.1103/RevModPhys.39.125.
[41] N. Rajiv, B.W. Sejpal, EMA modelled alternative EUV absorber materials considering optical and stability behavior, Proc. SPIE 11855 (2021) 2021, https://doi.org/10.1117/12.2600735.
[42] A.J. McEvoy, "ESCA spectrum and band structure of ruthenium chloride," in June 16, De Gruyter, 1982, pp. 569–574, https://doi.org/10.1515/9783112500682-033.
[43] A. Jain, et al., Commentary: the materials project: a materials genome approach to accelerating materials innovation, APL Mater. 1 (1) (2013), 011002, https://doi.org/10.1063/1.4812323.
[44] S. Speakman, "Basics of X-RAY Powder Diffraction," training document "Mit.edu, http://prism.mit.edu/xray/oldsite/Basics%20of%20X-Ray%20Powder%20Diffraction.pdf. Accessed 8 Jan. 2023.
[45] "Sample Preparation – EAS X-Ray Diffraction Laboratory – University of Alberta." Ualberta.Ca, https://cms.eas.ualberta.ca/xrd/sample-preparation/. Accessed 8 Jan. 2023.
[46] Materials data on Ru by materials project, in: LBNL Materials Project; Lawrence Berkeley National Laboratory (LBNL), Berkeley, CA (United States), 2020, https://doi.org/10.17188/1206459.
[47] Materials data on ta by materials project, in: LBNL Materials Project; Lawrence Berkeley National Laboratory (LBNL), Berkeley, CA (United States), 2020, https://doi.org/10.17188/1208553.
[48] Materials data on TaRu by materials project, in: LBNL Materials Project; Lawrence Berkeley National Laboratory (LBNL), Berkeley, CA (United States), 2020, https://doi.org/10.17188/1191510.
[49] Materials data on TaRu by materials project, in: LBNL Materials Project; Lawrence Berkeley National Laboratory (LBNL), Berkeley, CA (United States), 2020, https://doi.org/10.17188/1188588.
[50] XRD Crystallite (grain) Size Calculator (Scherrer Equation) - InstaNANO. https://instanano.com/all/characterization/xrd/crystallite-size/(accessed January 8th, 2023).
[51] K. He, et al., Method for determining crystal grain size by X-ray diffraction, Cryst. Res. Technol. 53 (2) (2018) 1700157, https://doi.org/10.1002/crat.201700157.
[52] Origin, "Version 2019". OriginLab Corporation, Northampton, MA, USA.
[53] W.S. Rasband, U.S. ImageJ, National Institutes of Health, Bethesda, Maryland, USA. https://imagej.nih.gov/ij/, 1997–2018.
[54] Vu Luong, et al., Optimized EUV mask absorber stack for improved imaging by reducing roughness and crystallinity of alternative absorber materials, in: Proc. International Symposium on Extreme Ultraviolet Lithography, 2016.
[55] T. Shimomura, T. Liang, Chemical durability studies of Ru-capped EUV mask blanks, in: H. Kawahira, L.S. Zurbrick (Eds.), Photomask Technology, 2008, https://doi.org/10.1117/12.803065.
[56] T.A. Theron, et al., Dissolution and quantification of tantalum-containing compounds: comparison with niobium, South African J. Chem. Suid-Afrikaanse Tydskrif Vir Chemie 64 (2011) 173–178. http://www.scielo.org.za/scielo.php?script=sci_arttext&pid=S0379-43502011000100025.
[57] R. P. Singh and M. J. Miller, "Method for the dissolution and purification of tantalum pentoxide (Patent No. 5635146)," in US Patent (1997).
[58] L. Ben, et al., Ta2O5 coating as an HF barrier for improving the electrochemical cycling performance of high-voltage spinel LiNi0.5Mn1.5O4 at elevated temperatures, ACS Appl. Energy Mater. acsaem.8b01139 (2018), https://doi.org/10.1021/acsaem.8b01139.
[59] J.H. Han, et al., Chemical vapor deposition of Ru thin films with an enhanced morphology, thermal stability, and electrical properties using a RuO4 precursor, Chem. Mater. A Pub. Am. Chem. Soc. 21 (2) (2009) 207–209, https://doi.org/10.1021/cm802485r.
[60] H.-Y. Lee, et al., Characteristics of sputter-deposited Ru thin films on Si substrates, Mater. Chem. Phys. 82 (3) (2003) 984–990, https://doi.org/10.1016/j.matchemphys.2003.08.022.
[61] Y. Abe, et al., Improvement of the crystal orientation and surface roughness of Ru thin films by introducing oxygen during sputtering, Jpn. J. Appl. Phys. 43 (1) (2008) 277–280 (2004), https://doi.org/10.1143/jjap.43.277.
[62] S.-H. Kwon, et al., Improvement of the morphological stability by stacking RuO [sub 2] on Ru thin films with atomic layer deposition, J. Electrochem. Soc. 154 (9) (2007) H773, https://doi.org/10.1149/1.2750448.
[63] C. van Lare, et al., "investigation into a prototype extreme ultraviolet low-n attenuated phase-shift mask," J. Micro/Nanopattern, Mats. Metro. 20 (02) (2021), https://doi.org/10.1117/1.JMM.20.2.021006.
[64] L.S. Melvin, et al., Impact of EUV mask absorber sidewall angle on patterning robustness, in: N.M. Felix, K.A. Goldberg (Eds.), Extreme Ultraviolet (EUV) Lithography IX, SPIE, 2018, https://doi.org/10.1117/12.2296865.

[65] M. Sugawara, I. Nishiyama, Impact of slanted absorber side walls on critical dimension error in extreme ultraviolet lithography, Jpn. J. Appl. Phys. 46 (1) (2008) 84–90 (2007), https://doi.org/10.1143/JJAP.46.84.
[66] Mack, C. A. (n.d.). Using the Normalized Image Log-Slope. Lithoguru.com. Retrieved August 19, 2022, from http://www.lithoguru.com/scientist/litho_tutor/TUTOR32%20(Winter%2001).pdf.
[67] E. van Setten, et al., High-NA EUV imaging: From system introduction towards low-k1 extension, in: K.G. Ronse, et al. (Eds.), International Conference on Extreme Ultraviolet Lithography 2021, SPIE, 2021, https://doi.org/10.1117/12.2600965.
[68] M. Burkhardt, A. Raghunathan, Best focus shift mechanism for thick masks, in: O. R. Wood, E.M. Panning (Eds.), Extreme Ultraviolet (EUV) Lithography VI, SPIE, 2015, https://doi.org/10.1117/12.2085948.
[69] D. Thakare, et al., Evaluation of Ta-Co alloys as novel high-k extreme ultraviolet mask absorber, J. Micro/Nanopattern. Mats. Metro. 22 (02) (2023), https://doi.org/10.1117/1.JMM.22.2.024403.
[70] A. Erdmann, et al., Mask-induced best-focus-shifts in DUV and EUV lithography, in: K. Lai, A. Erdmann (Eds.), Optical Microlithography XXVIII, SPIE, 2015, https://doi.org/10.1117/12.2086346.
[71] J. Finders, L. de Winter, T. Last, Mitigation of mask three-dimensional induced phase effects by absorber optimization in ArFiand extreme ultraviolet lithography, J. Micro. Nanolithogr. MEMS MOEMS 15 (2) (2016), 021408, https://doi.org/10.1117/1.JMM.15.2.021408.
[72] H. Mesilhy, et al., EUV mask absorber induced best focus shifts, in: A. Lio, M. Burkhardt (Eds.), Optical and EUV Nanolithography XXXV, SPIE, 2022, https://doi.org/10.1117/12.2614174.
[73] M. Burkhardt, et al., Focus considerations of design pitches and absorber choice for EUV random logic, in: A. Lio, M. Burkhardt (Eds.), Optical and EUV Nanolithography XXXV, SPIE, 2022, https://doi.org/10.1117/12.2614296.
[74] A. Erdmann, H. Mesilhy, P. Evanschitzky, Attenuated phase shift masks: a wild card resolution enhancement for extreme ultraviolet lithography? J. Micro/Nanopattern. Mats. Metro. 21 (02) (2022) https://doi.org/10.1117/1.JMM.21.2.020901.
[75] A. Erdmann, et al., Perspectives and tradeoffs of absorber materials for high NA EUV lithography, J. Micro. Nanolithogr. MEMS MOEMS 19 (04) (2020), https://doi.org/10.1117/1.JMM.19.4.041001.
[76] K.-H. Ko, et al., Influence of a non-ideal sidewall angle of extreme ultra-violet mask absorber for 1 ×−nm patterning in isomorphic and anamorphic lithography, Microelectron. Eng. 181 (2017) 1–9.